Available online at www.sciencedirect.com

ScienceDirect

Geochimica et Cosmochimica Acta 296 (2021) 75–96

Geochimica et Cosmochimica Acta

www.elsevier.com/locate/gca

Petrographic and isotopic investigations of two unusual Ca-Al-rich inclusions from primitive CO3 chondrites

A.T. Hertwig [a,*], M.-C. Liu [a], A.J. Brearley [b], S.B. Simon [c]

[a] Department of Earth, Planetary, and Space Sciences, University of California, Los Angeles, Los Angeles, CA 90095, USA
[b] Department of Earth and Planetary Sciences, MSC03-2040, University of New Mexico, Albuquerque, NM 87131, USA
[c] Institute of Meteoritics, Department of Earth and Planetary Sciences, MSC03-2040, University of New Mexico, Albuquerque, NM 87131, USA

Received 15 July 2020; accepted in revised form 17 December 2020; available online 28 December 2020

Abstract

We performed high-precision SIMS (secondary ion mass spectrometry) ^{26}Al-^{26}Mg and oxygen isotope analyses of two unique CAIs, "Mesquite" and "Y24", found in the CO3.05 chondrites Northwest Africa 7892 and Yamato-81020, respectively. Mesquite is unusually large (~5 × 3 mm) for a CAI from any CO chondrite and exhibits a layered texture comprising a melilite-rich core surrounded by hibonite- and spinel-rich mantle layers and a semi-continuous spinel-dominated rim. The CAI Y24 stands out because of its distinct mineralogy: grossite, hibonite, and spinel are accompanied by abundant ultra-refractory-element-rich phases such as warkite, kangite, and perovskite. Silicates are absent in Y24.

Negatively fractionated δ^{25}Mg values of phases in the core and mantle layers of Mesquite suggest that the inclusion as a whole was never molten and, hence, represents an aggregate of condensates. The relatively large grain sizes of melilite in the core (up to ~300 μm) most likely are the result of solid-state recrystallization and coarsening of melilite in the course of a heating event occurring in the solar nebula. This heating event, however, did not disturb the Al-Mg systematics of Mesquite. Regardless of their position within Mesquite and the phases analyzed, spots analyzed for Al-Mg plot on a single isochron characterized by an initial ^{26}Al/^{27}Al of $(4.95 \pm 0.08) \times 10^{-5}$ and a δ^{26}Mg*$_0$ of -0.14 ± 0.05‰. We suggest that this initial ^{26}Al/^{27}Al ratio corresponds to the formation of Mesquite in the solar nebula that was slightly heterogeneous with respect to Mg isotopes. Spinel in the rim is uniform in Δ^{17}O (~–25‰); in contrast, hibonite in the core and mantle layers, albeit also ^{16}O-rich, show variable oxygen isotope ratios (Δ^{17}O ~ –15‰ to –23‰), which would be consistent with hibonite condensation in a gas with quickly-changing oxygen isotope compositions. The ^{16}O-poor composition of melilite (Δ^{17}O ~ –1‰ to 0‰) in the core could be the result of isotope exchange with an ^{16}O-poor gas, perhaps during the heating event that caused the solid-state recrystallization and coarsening of melilite or the result of oxygen isotope exchange with a fluid on the parent body. Abundant calcite, phyllosilicates, and sodalite are witnesses to late-stage and low-temperature alteration of the Mesquite CAI; calcite and phyllosilicates most likely are of terrestrial origin, but sodalite could have formed in the parent body.

Inclusion Y24 is irregularly-shaped, indicating a condensation origin. Completely enclosing other phases, warkite forms the matrix of Y24, which could be the result of simultaneous condensation and growth of warkite, grossite, and hibonite. Possibly, spinel formed by replacing grossite or hibonite or both minerals in a gradually cooling gas before any silicates condensed. SIMS analyses indicate that condensation occurred in an ^{16}O-rich gas when ^{26}Al/^{27}Al was $(5.4 \pm 1.0) \times 10^{-5}$.

* Corresponding author at: Universität Heidelberg, Institut für Geowissenschaften, Im Neuenheimer Feld 234-236, 69120 Heidelberg, Germany.
E-mail address: andreas.hertwig@geow.uni-heidelberg.de (A.T. Hertwig).

https://doi.org/10.1016/j.gca.2020.12.014

Oxygen isotope exchange with an ^{16}O-poor fluid in the parent body or with an ^{16}O-poor gas in a nebular setting caused the ^{16}O-poor compositions in grossite and kangite.

Keywords: Al-26; Oxygen isotopes; Calcium-aluminum-rich inclusions; CO chondrites

1. INTRODUCTION

Calcium-aluminum-rich inclusions (CAIs) – a ubiquitous component of most carbonaceous chondrites (CC) – are among the oldest solids formed in the solar nebula (e.g., Kita et al., 2005; Jacobsen et al., 2008; Amelin et al., 2010; Krot, 2019; MacPherson, 2014) and are especially abundant in the CO, CV, and CM chondrite groups (Scott and Krot, 2014, and references therein). The U-corrected Pb-Pb age of 4.567 ± 0.16 Ga for a set of CAIs from CV chondrites is taken as "the zero time point" (Amelin et al., 2010; Connelly et al., 2012, 2017) in the evolution of the protoplanetary disk. A timeline of events that occurred during the first few millions of years after this time zero, i.e., after CAI formation, can then be constructed by using relative dating methods, with the ^{26}Al-^{26}Mg radioactive decay system being the most utilized one (e.g., Kita et al., 2005). By measuring the excess of radiogenic ^{26}Mg due to the in situ decay of ^{26}Al (half-life: ~0.7 My, Norris et al., 1983) in meteoritic samples, it is possible to deduce the amount of time between time zero and the crystallization or formation of phases in these samples, provided that the initial abundance of ^{26}Al in the CAI-forming reservoir is known and it was homogeneously distributed in the CAI-forming region. In the past 15 years, high-precision in situ and bulk magnesium isotope measurements of large (>5 mm) CAIs from CV3 chondrites have revealed that many inclusions which have escaped post-formation isotopic disturbance show initial ^{26}Al/^{27}Al ratios ($\equiv(^{26}Al/^{27}Al)_0$) consistent with $5.2 \pm 0.1 \times 10^{-5}$, the so-called "canonical" value (e.g., Jacobsen et al., 2008; MacPherson et al., 2012, 2017). However, there are well-resolved variations in the $(^{26}Al/^{27}Al)_0$ of CAIs, all obtained through the internal isochron method, indicating (partial) melting of some inclusions and resetting of their Mg isotope systematics (e.g., MacPherson et al., 1995, 2012; Liu et al., 2019). Those variations play an important role in deducing the sequence of processes occurring in the nascent protoplanetary disk (e.g., Liu et al., 2019).

Processes involving gaseous and condensed materials can be traced by studying the oxygen isotopic composition of CAIs (e.g., Clayton et al., 1977; Krot and Nagashima, 2016; Ushikubo et al., 2017). Except for rare hibonite and corundum grains that do not carry fossil records of ^{26}Al but are ^{16}O-rich (e.g., Liu et al., 2009; Makide et al., 2011; Kööp et al., 2016), pristine refractory inclusions, including CAIs that were not affected by secondary processes, possess canonical $(^{26}Al/^{27}Al)_0$ and are predominantly ^{16}O-rich with $\Delta^{17}O$ ($=\delta^{17}O - 0.52 \times \delta^{18}O$) values ranging typically between –25‰ and –23‰ (Krot, 2019, and references therein). On the other hand, CAIs that experienced melting in the disk or secondary alteration on their parent-body asteroids often show heterogeneous, mineralogically-controlled (Krot, 2019) oxygen isotopic compositions (Kawasaki et al., 2017; Krot et al., 2019c; Krot, 2019, and references therein); in such inclusions, analyses of, for instance, spinel and hibonite yield ^{16}O-rich compositions, whereas minerals such as melilite and anorthite are usually ^{16}O-poor relative to the aforementioned phases (Krot, 2019). Further, there is evidence for isotopically distinct gaseous reservoirs that were present during the era of CAI formation, as suggested by variable ^{16}O-enrichments of fine-grained inclusions (Yurimoto et al., 2008, and references therein) or ^{16}O-poor refractory oxides (e.g., Ivanova et al., 2012; Zhang et al., 2015) found in ultra-refractory (UR) inclusions.

Compared to those from CV chondrites, CAIs from CO chondrites are small (<500 μm, Russell et al., 1998). Common CAI types in CO chondrites include melilite-, hibonite-, and spinel-rich inclusions, whereas grossite- and pyroxene-rich types are uncommon (Scott and Krot, 2014, and references therein). As in other chondrites, CAIs rich in ultra-refractory-element-dominant minerals such as warkite [$Ca_2Sc_6Al_6O_{20}$] (Ma et al., 2015) or kangite [$(Sc,Ti,Al,Zr,Mg,Ca,\square)_2O_3$] (Ma et al., 2013) are extremely rare in CO chondrites. In 2012, only 13 ultrarefractory (UR) inclusions were tabulated by Ivanova et al. (2012). More UR inclusions have been found in the course of the following years (e.g., Ma et al., 2012, 2015); a recent compilation of UR inclusions by Krot et al. (2019a) lists 34 such inclusions known to date. Although no rare earth element (REE) patterns have been obtained for most of these inclusions, it is probable that most of them are characterized by ultra-refractory patterns (enriched in heavy REEs, Boynton, 1989) judging from the high abundance of minerals rich in ultra-refractory elements (Krot, 2019).

Here we report on two special CAIs found in two different CO3.0 chondrites. The first CAI, "Mesquite", was found in the newly described CO3.05 chondrite Northwest Africa 7892. This inclusion is melilite-rich with a layered structure. It stands out because its size of ~5 mm is much larger than those of most CO CAIs. The second CAI of interest, "Y24", is from the Yamato(Y)-81020 chondrite, and is peculiar due to its distinct mineralogy. The isolated inclusion Y24 is composed of abundant ultra-refractory-element-rich minerals such as warkite, kangite, and perovskite in combination with grossite, hibonite, and spinel.

Because of their unique features, we investigated both inclusions petrographically using scanning electron microscopy (SEM) and determined their Al-Mg and O isotope systematics using secondary ion mass spectrometry (SIMS). The large size and layered structure of Mesquite offer an opportunity to check for possible differences in the formation environments and times between minerals in different

layers. The isotope data in combination with the special mineralogy of Y24 will provide some insights into the chronology and conditions in which UR-element-rich inclusions formed.

2. ANALYTICAL METHODS

2.1. Samples and electron microscopy

The CAI Mesquite is from an epoxy-mounted thick section of the NWA 7892 chondrite (The Meteoritical Bulletin, No. 102) that was purchased from a meteorite dealer in 2012; the studied section is a loan from the Center for Meteorite Studies of the Arizona State University (ASU). The ultra-refractory-element-rich CAI Y24 was discovered in a thin section of the Y-81020 chondrite (section number #61-6) that was provided to us by the National Institute of Polar Research (NIPR), Japan.

Initial secondary electron (SE) and backscattered electron (BSE) images of Mesquite were acquired using the JEOL JXA-8530F electron microprobe at Arizona State University (ASU). Additional imagery of Mesquite as well as electron images of Y24 were obtained using the Tescan Vega-3 XMU scanning electron microscope located at the University of California, Los Angeles (UCLA). Qualitative elemental distribution maps (X-ray maps) of Ca (Kα), Al (Kα), and Mg (Kα) of Mesquite, and Ca (Kα), Al (Kα), Mg (Kα), Ti (Kα), Zr (Lα), and Sc (Kα) of Y24 were made at ASU and UCLA, respectively.

Chemical compositions of minerals were determined during two analytical sessions using the JEOL JXA-8200 Superprobe at UCLA (15 kV, 15 nA). In the first session, melilite, hibonite, and spinel in Mesquite were analyzed for concentrations of SiO_2, TiO_2, Al_2O_3, Cr_2O_3, MgO, FeO, CaO, MnO, Na_2O, and K_2O. The counting time on the peaks was 20 seconds (5 seconds on background) for all elements except Na and K (10 and 5 seconds, respectively, on background). The following reference materials (standards) were used to calibrate the X-ray response for the various elements: anorthite (Si, Al, Ca), sphene (Ti), chromium spinel (Cr), forsterite (Mg), magnetite (Fe), MNGA (Mn), albite (Na), and GKFS (K).

In the second session, the mineral chemistry of hibonite, grossite, spinel, and those of refractory-element-rich oxides in Y24 were determined by measuring SiO_2, TiO_2, ZrO_2, HfO_2, Al_2O_3, Cr_2O_3, Sc_2O_3, Y_2O_3, V_2O_3, MgO, FeO, and CaO contents. The counting time on the peaks was 20 seconds (5 seconds on background) for all elements except Cr (60 seconds on the peak and 15 seconds on the background) and Y (30 seconds for both the peak and the background). The following reference materials were used in the second session: forsterite (Si, Mg), sphene (Ti), zircon (Zr), hafnon (Hf), anorthite (Al, Ca), chromium spinel (Cr), $ScPO_4$ (Sc), YPO_4 (Y), VOx (V), and magnetite (Fe).

2.2. Ion microprobe analyses

Oxygen and magnesium isotope analyses were performed using the CAMECA ims-1290 ion microprobe at UCLA during 9 analytical sessions (4 for oxygen isotopes, 5 for magnesium isotopes). For magnesium isotope analysis of Y24, locations of SIMS measurements were marked by a focused ion beam (FIB) instrument. All of the SIMS pits were imaged by SEM to check for pit imperfections and accuracy of aiming (see Electronic Annex EA1).

2.2.1. Location of SIMS measurements and marking by FIB

Locations of prospective SIMS analyses were chosen based on high-resolution secondary electron (SE) and backscattered electron (BSE) images. In the case of inclusion Y24, the small sizes of individual phases would have made it difficult to aim accurately the primary ion beam by using the optical microscope of the Cameca ims-1290 alone. Therefore, for magnesium isotope analysis, locations of interest were marked before analysis by using the Nova 600 NanoLab SEM/FIB instrument of the UCLA Nanoelectronics Research Facility (NRF). The general procedure follows descriptions in Nakashima et al. (2012) and Defouilloy et al. (2017). A Ga^+ beam (30 kV, 10 pA) was rastered over the sample surface for approximately 60 seconds to remove the carbon coating from a 1 μm × 1 μm area on top of the prospective measurement location. Subsequently, SE images were acquired to document the precise location of the FIB marks. During magnesium isotope analysis with the Cameca ims-1290, scanning ion images (Al^+) of different raster sizes, which were obtained with a low primary beam current (~50 pA) to limit sputtering of the carbon coating, were used to position the primary ion beam exactly over the FIB marks.

2.2.2. Oxygen isotope analysis

We acquired the oxygen isotopic composition of minerals in Y24 and Mesquite in four separate sessions (O3-I, O3-II, O3-III, O3-IV). In sessions O3-I and -II, a primary Cs^+ beam (Gaussian mode) of ~20 pA was focused on the sample surface resulting in a pit ~5 μm in diameter. Intensities of $^{16}O^-$, $^{17}O^-$, and $^{18}O^-$ signals were measured simultaneously using one Faraday cup (FC) on the multi-collection detector array, the axial electron multiplier (EM), and another EM on the detector array, respectively. The mass resolving power (MRP) for $^{17}O^-$ was set to ~7000; the MRP for $^{16}O^-$ and $^{18}O^-$ on the multi-collection detector array was 2500. The secondary intensities of $^{16}O^-$ on the Madagascar hibonite (Madhib) standard were ~4×10^7 (O3-I) or ~2.7×10^7 (O3-II) cps due to different magnification settings in the transfer optics. Data were acquired over 20 cycles of 10 seconds each, after pre-sputtering (90 or 120 seconds) and two centering routines (beam in the field aperture, magnetic field centering). The external reproducibility of the Madhib standard for $\delta^{17}O$, $\delta^{18}O$, and $\Delta^{17}O$ was 2.0, 0.7, and 2.0‰ (n = 7, 2SD) or 2.0, 1.5, and 2.5‰ (n = 6, 2SD) for session O3-I or O3-II, receptively.

In the third session (O3-III), a primary Cs^+ beam of ~4 nA was focused on the sample surface (Gaussian mode, ~10 μm, no raster) and secondary intensities were high enough (~3×10^9 cps for Madhib) to simultaneously detect ions using two FCs on the multi-collection array ($^{16}O^-$, $^{18}O^-$) and an axial FC ($^{17}O^-$). The MRP was similar to that in sessions O3-I and -II. Following pre-sputtering for 45

seconds and centering routines, data were measured over 10 cycles of 20 seconds each. External reproducibility of the Madhib standard over the entire session was 0.35, 0.82, and 0.26‰ (n = 9, 2SD) for $\delta^{17}O$, $\delta^{18}O$, and $\Delta^{17}O$, respectively.

In the fourth session (O3-IV), we analyzed secondary alteration products and calcite, which contain significant amounts of water in their crystal structure or within pores. Hence, the contribution of $^{16}OH^-$ to the $^{17}O^-$ signal is expected to be non-negligible. By scanning the low-mass side of the $^{18}O^-$ peak (0.0038 atomic mass units below the nominal ^{18}O mass, where there is no hydride contribution) with the axial EM, we estimated the ratio of the counts of the low-mass tail to the counts of the peak. To a first approximation, this ratio (1/77,000) adequately describes the shape for the $^{16}OH^-$ peak and is expected to stay constant regardless of the intensity of the peak. At the end of each analysis, the $^{16}OH^-$ signal was measured automatically by deflecting the beam into an axial FC using the DSP2-X deflector, similar to procedures applied by, e.g., Heck et al. (2010) and Kita et al. (2010, see their Supplementary data EA1). The contribution of the hydride tail to the $^{17}O^-$ signal was estimated based on the established ratio and typically a correction of 0.5‰ to 2‰ was applied. A primary Cs^+ beam of ~3 nA was used in the fourth session (Gaussian mode, ~12 μm, 3 μm raster). The collector configuration and MRP were the same as those in O3-III. Following pre-sputtering (30 seconds) and centering routines, data were measured over 10 cycles (each 20 s). The external reproducibility of the in-house calcite standard (McCain et al., 2018) over the entire session was 0.8, 1.2, and 0.5‰ (n = 12, 2SD) for $\delta^{17}O$, $\delta^{18}O$, and $\Delta^{17}O$, respectively.

Isotope ratios are expressed relative to Vienna Standard Mean Ocean Water (VSMOW, Baertschi, 1976). Corrections of isotope ratios of unknown samples for mass-dependent fractionation occurring in the instrument were carried out by comparing to standards of spinel (Burma spinel, Bsp; $\delta^{18}O = 22.30$‰), Madagascar hibonite (Madhib, $\delta^{18}O = 10.0$‰), and calcite ($\delta^{18}O = 11.1$‰, McCain et al., 2018). Additionally, San Carlos (SC) olivine and SC pyroxene or a quartz standard were measured to check instrument stability and isotope fractionation behavior. The external reproducibilities of $\delta^{17}O$, $\delta^{18}O$, and $\Delta^{17}O$ (mean of all analyses of the respective session) on Bsp, Madhib, and calcite were assigned to represent the analytical uncertainty for the corresponding unknowns. When no matrix-matched standards were available (e.g., for melilite, grossite, phyllosilicates), only $\Delta^{17}O$ values were calculated and the standard error of the mean on a cycle-by-cycle basis (internal error, 2SE) was assigned as the analytical uncertainty in these cases.

2.2.3. Magnesium isotope analysis

The Al-Mg systematics of inclusions were determined in five separate analytical sessions using an O^- (session MultiFC-I) or O_3^- (sessions MultiFC-II, III, MonoEM-I, -II) primary ion beam generated by a Hyperion-II oxygen plasma source (Liu et al., 2018). For sessions MultiFC-I to -III, primary ion currents of 1, 3, or 5 nA (sizes of SIMS pits: 3–10 μm) yielded secondary ion intensities of $^{24}Mg^+$, $^{25}Mg^+$, $^{26}Mg^+$, and $^{27}Al^+$ strong enough (e.g., 5 nA, $^{24}Mg^+$: ~1.2×10^8 cps for Bsp, ~0.2×10^8 cps for Madhib) to be detected simultaneously using FCs on the multi-collection detector array. Interferences of $^{48}Ca^{2+}$ and $^{48}Ti^{2+}$ were separated from $^{24}Mg^+$ by setting the instrument to a MRP of ~2500 (exit slit 1 on the multi-collection array, 500 μm). This setting does not allow complete separation of $^{24}MgH^+$ from the $^{25}Mg^+$ signal; however, for sessions MultiFC-I and -II, the hydride contribution to the $^{25}Mg^+$ signal was minimal due to the high vacuum in the analysis chamber (<1×10^{-8} torr). In session MultiFC-III, vacuum in the analysis chamber was degraded, making it necessary to reduce the exit slit width (exit slit 2, 250 μm, corresponding to MRP of ~4500) to separate the hydride peak from the $^{25}Mg^+$ signal. After pre-sputtering for 60, 90, or 120 seconds and centering of the beam into the field aperture and the magnet field on the central FC, data acquisition was done in 10, 20, or 30 cycles (mostly dependent on the phase analyzed) with a 15-second counting time per cycle.

In sessions MonoEM-I and -II, primary beam currents of 90 or 250 pA and 30–50 pA, respectively, resulted in secondary ion intensities of magnesium isotopes suitable to be detected by the axial EM in pulse counting mode using magnetic field switching. Aluminum was collected on the axial FC2 detector. Counting times were 2, 8, 6, and 2 seconds for $^{24}Mg^+$, $^{25}Mg^+$, $^{26}Mg^+$, and $^{27}Al^+$, per cycle, respectively, with 10, 20, or 40 cycles per analysis. Pre-sputtering of the sample lasted 150 seconds and was followed by two centering routines (beam in the field aperture and magnetic field). The mass spectrometer was set to achieve a MRP of ~5000 using an exit slit width of 150 μm).

Terrestrial standards (San Carlos olivine, San Carlos pyroxene, Burma spinel, and Madagascar hibonite) were measured in sessions MultiFC-I to -III to characterize and correct for mass-dependent instrumental isotope fractionation during analysis, assuming the true isotopic compositions for the standards to be 0.12663 for $^{25}Mg/^{24}Mg$ and 0.13932 for $^{26}Mg/^{24}Mg$ (Catanzaro et al., 1966). Instrumental mass fractionation (α) inferred from standards is defined as:

$$\alpha_{25} = \frac{(^{25}Mg/^{24}Mg)_m^{std}}{0.12663} \quad \text{and} \quad \alpha_{26} = \frac{(^{26}Mg/^{24}Mg)_m^{std}}{0.13932},$$

where *m* stands for "measured". Deviations of the measured magnesium isotope ratios from the reference values were expressed in δ-notation:

$$\delta^{25}Mg = (\alpha_{25} - 1) \times 1000$$

$$\delta^{26}Mg = (\alpha_{26} - 1) \times 1000$$

The mass dependent fractionation of magnesium in the unknowns was calculated by correcting for mineral-specific IMF:

$$\delta^{25}Mg^{unk} = \left[\frac{(^{25}Mg/^{24}Mg)_m^{unk}/\alpha_{25}}{0.12663} - 1\right] \times 1000$$

It should be pointed out that the assumption that all standards are characterized by $\delta^{25}Mg = \delta^{26}Mg = 0$‰ may be inappropriate for those that were not of mantle origin,

such as Burma spinel and Madagascar hibonite, and therefore could potentially result in a $1-2‰$ systematic error on $\delta^{25}Mg$ of unknown samples (e.g., Young and Galy, 2004). However, such a level of inaccuracy is insignificant for the purpose of interpreting the formation mechanisms of the inclusions.

To characterize the fractionation behavior of the instrument, an exponential mass fractionation law

$$\left(1+\frac{\delta^{25}Mg}{1000}\right)=\left(1+\frac{\delta^{26}Mg}{1000}\right)^{\beta}$$

was applied, and for each of the multi-FC sessions (I, II, and III) one β value (0.515, 0.513, and 0.516) was derived by linear regression of standard measurements (only SC olivine, SC pyroxene, Bsp). Analyses performed during sessions MonoEM-I and -II were reduced using a constant β of 0.5128 (Davis et al., 2015).

If minerals in the inclusions incorporated ^{26}Al during their formation, their $^{26}Mg/^{24}Mg$ ratios would be deviated from those expected from the measured non-radiogenic $^{25}Mg/^{24}Mg$ ratio and the effect of mass-dependent fractionation. This excess in ^{26}Mg, denoted $\delta^{26}Mg^*$, is calculated by

$$\delta^{26}Mg^{*}=\delta^{26}Mg-\left[\left(1+\frac{\delta^{25}Mg}{1000}\right)^{1/\beta}-1\right]\times 1000$$

Relative sensitivity factors (RSFs) of $^{27}Al/^{24}Mg$, defined as $(^{27}Al/^{24}Mg)_m/(^{27}Al/^{24}Mg)_{true}$, were deduced by analysis of terrestrial standards (true $^{27}Al/^{24}Mg$ of Bsp: 2.56; Madhib: 25.2, Liu et al., 2009) and of a synthetic melilite glass (Ak_{20}; true $^{27}Al/^{24}Mg$ ratio: 10.4). RSF values are tabulated in the Electronic Annex EA1. The RSF value of the melilite glass was applied to the grossite data reduction. The 2-sigma external reproducibility of $\delta^{26}Mg^*$ was between 0.04 and 0.14‰ on the Bsp (MultiFC-I to III) and between 0.3 and 0.5‰ on the Madhib standard (MultiFC-I and -II). On the melilite glass, external reproducibility was ~1.5‰ (MonoEM-I) and ~1.0‰ (MonoEM-II).

The uncertainties in $\delta^{25}Mg$, $\delta^{26}Mg$, and $\delta^{26}Mg^*$ of unknowns were calculated by adding in quadrature the in-run variation (internal error) of individual analyses and the standard error of the mean of the respective standard measurements. For the uncertainty in $^{27}Al/^{24}Mg$, the procedure is similar except that the respective relative statistical quantities were used. Isochron regression was performed by using a Python implementation of the Mahon regression algorithm (Mahon, 1996; Trappitsch et al., 2018). Uncertainties on slope and intercept are the 95%-confidence intervals (no "overdispersion" applied) by using a t-value appropriate for the degrees of freedom of the regression.

3. RESULTS

3.1. Petrography and mineral chemistry

Mesquite is a large (5 mm × 3 mm), layered, melilite-rich inclusion from the NWA 7892 CO3 chondrite. Besides melilite, the inclusion comprises hibonite, spinel, perovskite, and secondary phases such as calcite, phyllosilicates, and sodalite. EDS x-ray mapping and BSE imaging (Fig. 1) reveal that the layered structure is concentric and composed of a melilite core (Figs. 1 and 2a, c) with domains of hibonite, a mantle (Fig. 2b) with layers of hibonite-spinel (±melilite), hibonite-melilite, and hibonite-melilite-perovskite, and a semi-continuous rim made of spinel and perovskite. The entire inclusion is surrounded by a fine-grained accretionary rim mainly comprising an unidentified Fe, Ca, Al-rich phase, finely dispersed Fe-oxides or hydroxides, and fine (a few μm) fragments of forsterite (Fig. 2d). The concentric layering is well-developed in the left half of the inclusion as shown in Fig. 1 but less apparent in the other half, possibly due to sectioning effects (Fig. 1b). This observation means that the inclusion is oriented in such a way that the hibonite-rich mantle and the spinel-rich rim were cut obliquely relative to the layering during

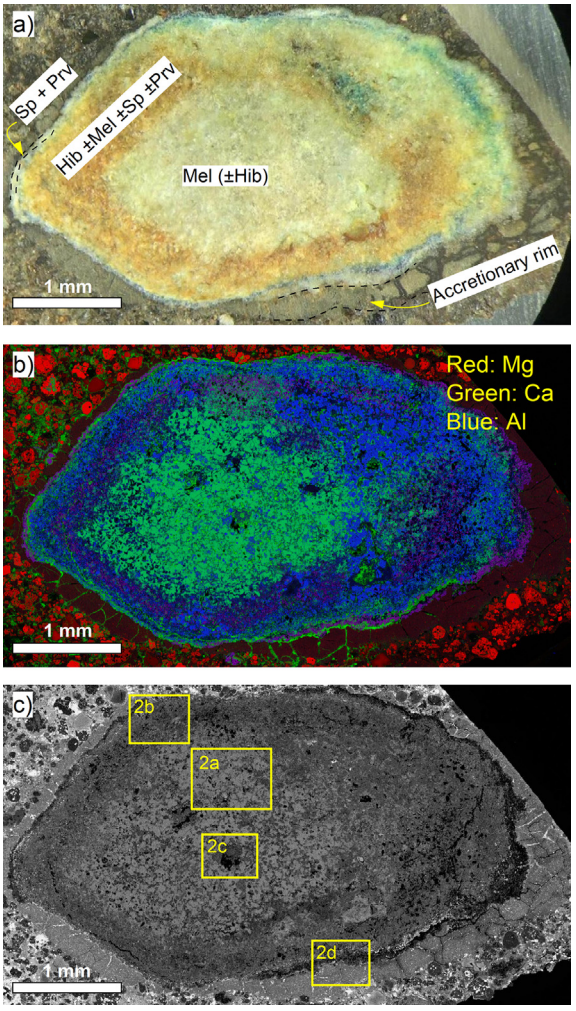

Fig. 1. Images of the Mesquite inclusion. (a) Optical light, (b) X-ray intensity, and (c) BSE images showing the general texture of Mesquite. The melilite-rich core is encased in a mantle consisting of hibonite, spinel, perovskite, as well as melilite. Core and mantle are themselves partially surrounded by a spinel-rich rim, and the whole inclusion is encased in an accretionary rim. Rectangles in (c) show locations of BSE images in Fig. 2. Mel: melilite, Hib: hibonite, Sp: spinel, Prv: perovskite. Scale bars in all images are 1 mm.

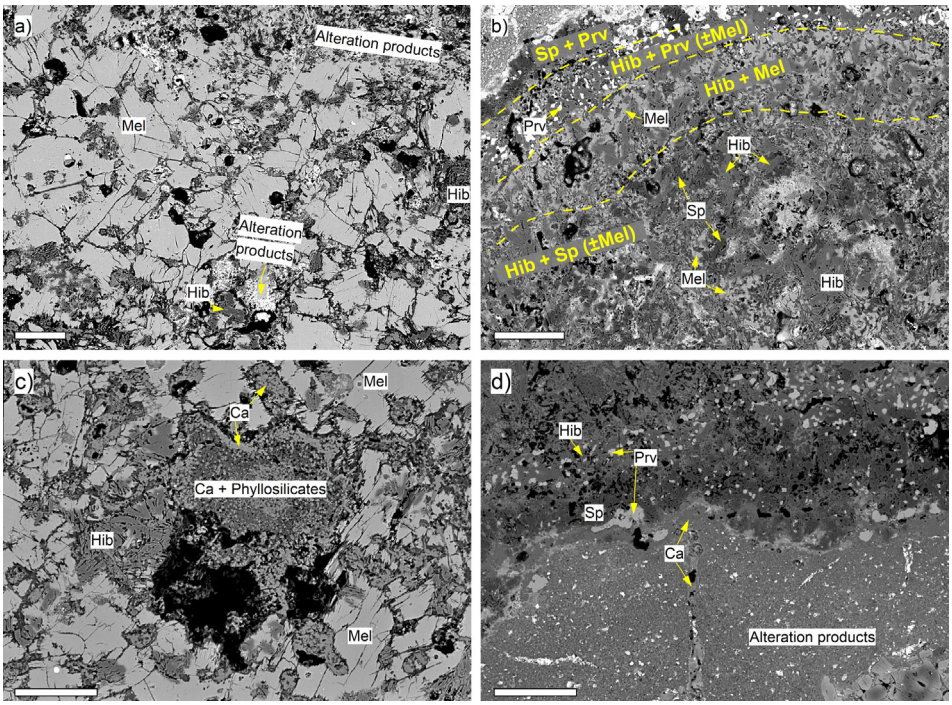

Fig. 2. BSE images showing the (a) texture of melilite in Mesquite's core, (b) sequence of mantle layers, (c) alteration textures associated with hibonite domain in the core, and (d) veined accretionary rim. Ca: calcite, other abbreviations as in Fig. 1. For location of BSE images see also Fig. 1c. Scales bars are 100 μm.

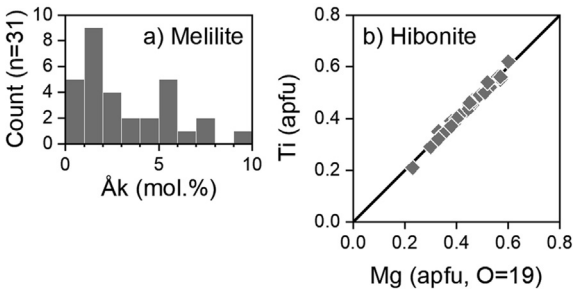

Fig. 3. Graphs showing mineral chemistry of (a) melilite and (b) hibonite in Mesquite. Melilite is gehlenitic with åkermanite contents < 10 mol.%. (b) Variations in mineral chemistry of hibonite can be explained by the coupled substitution $(MgTi^{4+})(2Al)_{-1}$. apfu: atoms per formula unit.

thick section preparation and therefore these layers exhibit a wider apparent thickness. The hibonite domains in the melilite core might therefore be actually part of the hibonite-rich mantle (Fig. 2c).

Melilite grains in the core are up to ~300 μm in size (Fig. 2a). Melilite in the mantle forms overgrowths (<10 μm) on often subhedral hibonite and fills spaces between hibonite grains. The åkermanite content of melilite ranges from ~0 to 10 mol.% (Fig. 3a, Table 1) regardless of whether melilite is located in the inclusion's core or in the mantle layers. Magnesium contents of hibonite are between 0.2 and 0.6 apfu (atoms per formula unit, based on 19 O, Fig. 3b, Table 1). Most variability in the hibonite chemistry can be explained by the coupled substitution $(MgTi^{4+})(2Al)_{-1}$. Spinel in the mantle and rim is near-endmember $MgAl_2O_4$.

Mesquite suffered significant low-temperature alteration. Secondary minerals formed along grain boundaries and voids in the melilite-rich core (Fig. 2a) and in the inclusions' mantle and rim. Hibonite domains in the core of the inclusion show evidence for alteration and formation of calcite and phyllosilicates (Fig. 2c). Further, calcite fills the veins that cut the accretionary rim, and x-ray mapping shows a Ca-rich chondrite matrix close to these still-filled veins (Figs. 1b and 2d). On the other hand, veins in the accretionary rim on the right half of the inclusion are free of alteration products and the adjacent chondrite matrix is less Ca-rich (Fig. 1b). Sodalite, confirmed by EDS analyses, is present in the mantle layers.

Inclusion Y24 measures approx. 300 μm × 150 μm, is irregularly shaped, and comprises grossite, spinel, and hibonite as well as ultra-refractory-element-rich oxides such as warkite, kangite, and perovskite (Fig. 4a). All phases are encased in warkite, which forms the matrix of this inclusion (Figs. 4 and 5a). Subhedral laths of grossite are located close to the inclusion's margins and do not show a preferred orientation within the inclusion. They possess undulant grain boundaries with warkite. Spinel is either located close to the edges of grossite laths or is part of the laths itself; spinel crystals in the lower left of the inclusion (Fig. 4) are lath-shaped. One single, subhedral hibonite crystal is present in Y24 and it shares a straight grain boundary with adjacent spinel (Fig. 5a). Three different Sc, Zr, Ti-rich oxides were identified. Kangite, with Sc as the dominant cation, and a HREE-rich perovskite form clusters of inter-

Table 1
Mineral chemistry of phases in Mesquite from NWA 7892.

No.	1	2	3	4	5	6	7	8	9	10	11
Mineral	Melilite	Melilite	Melilite	Melilite	Hibonite	Hibonite	Hibonite	Hibonite	Spinel	Spinel	Spinel
wt.%											
SiO_2	24.13	22.76	23.89	21.62	0.41	0.25	0.34	0.39	0.05	0.03	0.04
TiO_2	0.00	0.04	0.00	0.07	5.23	6.70	2.53	6.72	0.06	0.15	0.10
Al_2O_3	33.76	36.27	34.37	36.04	82.15	82.06	87.31	82.04	71.81	71.84	71.62
Cr_2O_3	0.01	0.05	0.00	0.00	0.00	0.03	0.02	0.00	0.15	0.05	0.10
MgO	1.35	0.38	1.01	0.05	2.70	3.34	1.39	3.43	27.87	27.62	27.41
FeO	0.00	0.00	0.00	0.03	0.02	0.02	0.06	0.07	0.36	0.26	0.84
MnO	0.01	0.01	0.01	0.03	0.02	0.00	0.00	0.00	0.07	0.06	0.02
CaO	41.36	41.26	41.35	40.88	8.65	8.44	8.56	8.59	0.14	0.09	0.08
Na_2O	0.00	0.00	0.00	0.00	0.01	0.00	0.00	0.01	0.00	0.00	0.00
K_2O	0.00	0.00	0.00	0.00	0.00	0.00	0.02	0.00	0.00	0.01	0.00
Total	100.61	100.76	100.63	98.72	99.19	100.84	100.22	101.24	100.50	100.12	100.21
apfu											
Si	1.09	1.03	1.08	1.00	0.05	0.03	0.04	0.04	0.00	0.00	0.00
Ti	0.00	0.00	0.00	0.00	0.45	0.56	0.21	0.56	0.00	0.00	0.00
Al	1.81	1.94	1.84	1.97	11.00	10.83	11.49	10.79	2.00	2.01	2.00
Cr	0.00	0.00	0.00	0.00	0.00	0.00	0.00	0.00	0.00	0.00	0.00
Mg	0.09	0.03	0.07	0.00	0.46	0.56	0.23	0.57	0.98	0.98	0.97
Fe	0.00	0.00	0.00	0.00	0.00	0.00	0.01	0.01	0.01	0.01	0.02
Mn	0.00	0.00	0.00	0.00	0.00	0.00	0.00	0.00	0.00	0.00	0.00
Ca	2.01	2.00	2.01	2.03	1.05	1.01	1.02	1.03	0.00	0.00	0.00
Na	0.00	0.00	0.00	0.00	0.00	0.00	0.00	0.00	0.00	0.00	0.00
K	0.00	0.00	0.00	0.00	0.00	0.00	0.00	0.00	0.00	0.00	0.00
Total	5.00	5.00	5.00	5.01	13.01	12.99	13.01	13.00	3.00	2.99	3.00
Ak	9.1	2.5	6.9	0.3	–	–	–	–	–	–	–
O	7	7	7	7	19	19	19	19	4	4	4

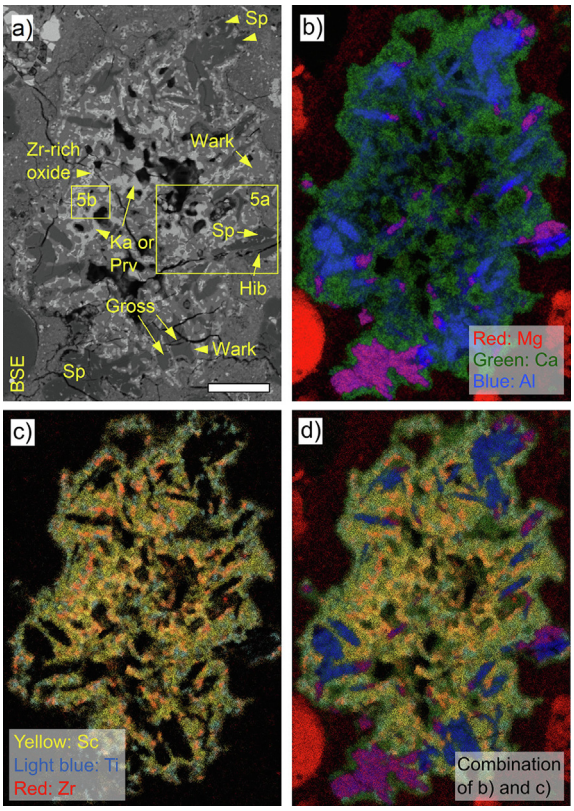

Fig. 4. (a) BSE image and (b-d) X-ray intensity maps of inclusion Y24 illustrating its irregular shape and texture. Spinel is located at the edges of grossite (Gross) laths. Laths themselves are encased in warkite (Wark) matrix. Refractory-element-rich oxides (Ka: kangite, Prv: perovskite) form clusters. Rectangles in (a) show position of images in Fig. 5. Scale bar in (a) is 50 μm.

connected grains (individual grains: <~5 μm) in the inclusion's interior (Fig. 5a). Sizes of these clusters decrease towards the margins of the inclusion. The third oxide is finer-grained, Zr-rich (BSE-bright) and subordinate in abundance to the other two oxides. Clusters or chains of oxides tend to be aligned with grossite laths or with the curvature of the inclusion's margins.

Electron probe microanalysis (EPMA) results (Table 2) show that warkite (endmember: $Ca_2Sc_6Al_6O_{20}$) contains significant amounts of Ti (up to 0.7 apfu), Zr (0.3 apfu), Mg (0.3 apfu), and Y (0.1 apfu). Given the stoichiometric constraints (20 O, cation total of 14), most Ti in warkite is trivalent. This is not uncommon for warkite (Ma et al., 2020). Grossite composition is that of the endmember ($CaAl_4O_7$). Aluminum spinel contains negligible amounts of Fe (~0.1 apfu). The Sc-rich oxide in Y24 exhibits a higher Sc/Ti ratio than the kangite described by Ma et al. (2013) (Fig. 6). However, since Sc is the major trivalent cation and trivalent cations are overall dominant (Sc + Al + Y: ~1.2 apfu; Ti^{4+}+Ca + Zr: ~0.7 apfu; based on 3 O), this Sc-rich oxide can be best termed kangite (Ma et al., 2013). EDS analyses show the presence of Gd, Dy, and Er in perovskite, which explains the low oxide totals of EPMA analyses (see Table 2). Qualitative EDS x-ray mapping indicates that the BSE-bright, fine-grained oxide phase is very Zr-rich; no accurate chemical composition was determined because of the small grain sizes.

3.2. Oxygen isotopes

Spinel grains in Mesquite are characterized by $\Delta^{17}O$ values of ~–25‰ (Fig. 7a); in comparison, hibonite is more variable in $\Delta^{17}O$ (–23‰ to –15‰) (Table 3). Some small part of this variability might be due to the primary ion beam hitting pores and cracks, potentially filled with secondary phases (see Electronic Annex EA1), but as will be argued later, the oxygen isotopic composition of hibonite most likely was inherited from the gas reservoirs. The oxygen isotopic compositions of spinel and hibonite in Mesquite plot on or close to the carbonaceous chondrite anhydrous mineral (CCAM) line on the oxygen three-isotope diagram (Fig. 7b). Calcite was found to plot on the TF line, as was the unknown secondary phase that forms intergrowths with calcite in hibonite domains from the core of the inclusion. The $\Delta^{17}O$ values of sodalite are either indistinguishable from 0‰ or slightly more ^{16}O-rich. The accretionary rim is slightly more ^{16}O-rich ($\Delta^{17}O \sim -2.5$‰) than the sodalite.

Spinel in Y24 is also ^{16}O-rich (–17‰ to –20‰, see Fig. 8 and Table 4). Warkite was found to be indistinguishable from spinel in terms of $\Delta^{17}O$, whereas grossite is either ^{16}O-poor (–2‰) or ^{16}O-rich (–18‰, mixture with warkite). The ^{16}O-poor composition of grossite in Y24 is in line with findings of a previous study of a grossite-beaing CAI from Y-81020 (Krot et al., 2019b). Kangite was found to be ^{16}O-poor, with $\Delta^{17}O$ values of 0‰ and –5‰ (n = 2).

3.3. Al-Mg systematics

We analyzed melilite and hibonite in the core and mantle of Mesquite as well as spinel in the mantle and rim layers of the inclusion, with $^{27}Al/^{24}Mg$ ratios of ~2.7 for spinel, 23–46 for hibonite, and 32–342 for melilite (Table 5). All phases analyzed in the different layers showed evidence for incorporation of live ^{26}Al during their formation and plot on a single, well-defined isochron (Fig. 9). The slope of this isochron corresponds to an $(^{26}Al/^{27}Al)_0$ of $(4.95 \pm 0.08) \times 10^{-5}$; the intercept is -0.14 ± 0.05‰, resolvable from zero (MSWD = 2.4, 95%-confidence intervals, Fig. 9). Further, individual isochrons using just melilite from the core [$(5.07 \pm 0.35) \times 10^{-5}$; -0.03 ± 2.13‰; MSWD = 1.92; 95%-confidence intervals], analyses of both the melilite and hibonite from the core [$(5.10 \pm 0.26) \times 10^{-5}$; -0.45 ± 0.66‰; MSWD = 1.43; 95%-confidence intervals] or just analyses of the mantle layers [$(4.95 \pm 0.11) \times 10^{-5}$; -0.19 ± 0.18‰; MSWD = 3.8; 95%-confidence] possess slopes and intercepts that are indistinguishable from each other.

Mesquite is characterized by mostly negatively fractionated stable magnesium isotopes, with $\delta^{25}Mg$ values being distinguishable from zero for most minerals of the core and mantle layers (Fig. 10). On the other hand, analyses of spinel of the rim yielded either slightly positive $\delta^{25}Mg$ values or values that are indistinguishable from zero. Spinel from the mantle is significantly lighter than spinel in the

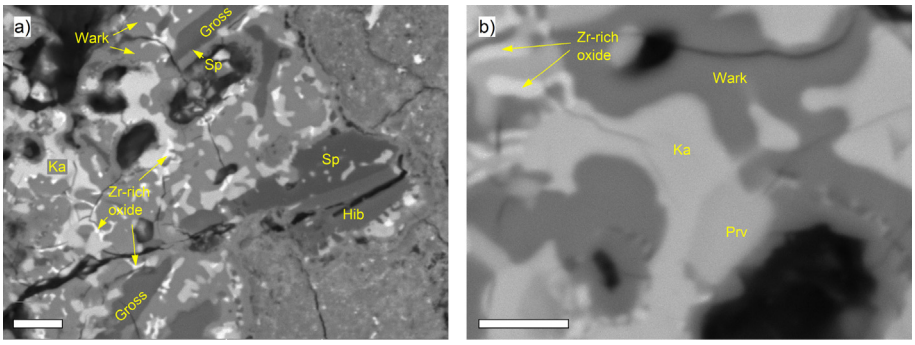

Fig. 5. BSE images of Y24 illustrating (a) grossite laths encased in warkite matrix and (b) intergrowth textures of refractory-element-rich oxides. For location of images within inclusion and mineral abbreviations see Fig. 4. Scale bars are 10 μm (a) and 5 μm (b).

Table 2
Mineral chemistry of phases in inclusion Y24 from Y-81020.

No.	1	2	3	4	5	6	7	8
Mineral	Hibonite	Spinel	Grossite	Warkite	Warkite	Kangite	Kangite	Perovskite
wt.%								
SiO_2	0.15	0.03	0.00	0.40	0.16	0.00	0.06	0.06
TiO_2	4.30	0.08	0.11	6.55	5.63	18.96	14.35	46.19
ZrO_2	0.26	0.04	0.00	3.52	4.26	18.61	26.79	4.60
HfO_2	0.12	0.00	0.04	0.26	0.33	0.42	0.61	0.28
Al_2O_3	82.86	69.96	79.02	38.72	38.15	11.16	9.27	3.54
Cr_2O_3	0.00	0.14	0.00	0.01	0.04	0.00	0.12	0.00
Y_2O_3	0.00	0.00	0.00	0.78	1.33	8.27	6.53	7.59
Sc_2O_3	0.39	0.09	0.40	33.78	34.19	39.81	39.06	3.81
MgO	2.29	27.90	0.06	1.33	0.98	0.02	0.04	0.00
FeO	0.26	0.30	0.14	0.16	0.08	0.03	0.02	0.04
CaO	8.09	0.08	20.78	14.71	13.97	1.55	3.39	29.61
Total	98.72	98.61	100.54	100.21	99.09	98.82	100.23	95.71[a]
apfu								
Si	0.02	0.00	0.00	0.06	0.02	0.00	0.00	0.00
Ti^{4+}	0.37	0.00	0.00	0.21	0.06	0.34	0.26	0.85
Ti^{3+}	–	–	–	0.48[b]	0.54[b]	–	–	–
Zr	0.01	0.00	0.00	0.24	0.29	0.21	0.31	0.05
Hf	0.00	0.00	0.00	0.02	0.03	0.00	0.00	0.00
Al	11.15	1.99	4.00	6.35	6.38	0.31	0.26	0.10
Cr	0.00	0.00	0.00	0.00	0.00	0.00	0.00	0.00
Y	0.00	0.00	0.00	0.06	0.10	0.10	0.08	0.10
Sc	0.04	0.00	0.01	4.10	4.23	0.82	0.82	0.08
Mg	0.39	1.00	0.00	0.28	0.21	0.00	0.00	0.00
Fe	0.02	0.01	0.00	0.02	0.01	0.00	0.00	0.00
Ca	0.99	0.00	0.96	2.19	2.12	0.04	0.09	0.77
Total	13.00	3.00	4.99	14.00	14.00	1.83	1.84	1.96
O	19	4	7	20	20	3	3	3

[a] HREE (Gd, Dy, and Er) present, as detected by EDS.
[b] Estimated based on stoichiometry.

rim. The $\delta^{25}Mg$ values of melilite and hibonite of the core are indistinguishable from those of the mantle. One melilite analysis of the mantle yielded a slightly positive $\delta^{25}Mg$ value.

All analyzed phases in Y24 (spinel, hibonite, grossite) show evidence for incorporation of live ^{26}Al during their formation (Fig. 11). The $\delta^{26}Mg^*$ values range from 0.81 ± 0.09‰ for spinel to 65 ± 8‰ for grossite. The corresponding lowest and highest $^{27}Al/^{24}Mg$ ratios are 2.68 ± 0.06 and 196 ± 23, respectively (Table 6). One should note that the true $^{27}Al/^{24}Mg$ ratios of unknown grossite analyses were calculated by using the RSF of the synthetic

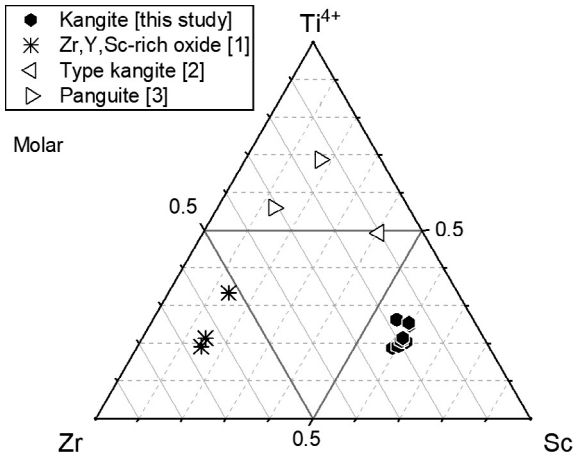

Fig. 6. Ternary diagram (mol percent) illustrating relative abundances of Zr, Ti, and Sc in different refractory-element-rich oxides found in CAIs. In comparison to the kangite described by Ma et al. (2013), kangite in Y24 in more Sc rich. Data from [1] Ivanova et al. (2012), [2] Ma et al. (2013), and [3] Ma et al. (2012).

melilite glass (Ak_{20}) because of the lack of a proper grossite RSF standard; therefore, most likely there would be a systematic error associated with this RSF correction, but the exact degree of such inaccuracy cannot be quantified. Isochron regression yielded an initial $^{26}Al/^{27}Al$ of $(5.4 \pm 1.0) \times 10^{-5}$ and $(\delta^{26}Mg^*)_0$ of $-0.22 \pm 0.27‰$ (MSDW = 3.0, n = 4, 95%-confidence intervals, Fig. 11). The $\delta^{25}Mg$ of hibonite is negatively fractionated ($-2.26 \pm 0.25‰$); that of spinel is indistinguishable from 0 ($0.10 \pm 0.12‰$).

4. DISCUSSION

In the following, the evolution of the Mesquite and Y24 inclusions will be discussed individually based on their textural and isotopic characteristics. Each of the inclusions is of particular interest and uncommon for CO chondrites: Mesquite stands out because of its size and texture; Y24, large for an isolated UR inclusion, is warkite-rich and comprises an assemblage of Si-free minerals.

4.1. Mesquite – one-of-a-kind inclusion from CO chondrites

Mesquite is substantially larger than CAIs that have been previously described in CO3 chondrites, which are typically <500 μm (e.g., Russell et al., 1998; Itoh et al., 2004; Han and Brearley, 2017; Mishra, 2018). The petrographic texture, mineralogy, and magnesium and oxygen isotopic compositions of this inclusion suggest that it had a complicated history of evolution in the solar nebula. Petrographically, although not "fluffy" or nodular, Mesquite shares a few similarities with fluffy Type A (FTA) inclusions from CV chondrites, such as its size, melilite-rich mineralogy (plus fine-grained hibonite, and spinel), irregular texture of the mantle minerals, the absence of blocky spinel, and the low åkermanite content ($Åk_{0–9}$) of melilite (e.g., MacPherson and Grossman, 1984, Brearley and Jones, 1998, and references therein; MacPherson, 2014). Isotopically, the slightly negatively fractionated stable Mg isotopes ($\delta^{25}Mg$) found throughout Mesquite (except for spinel in the outermost part of the rim) are also similar to those reported for FTA samples (e.g., MacPherson et al., 2012). These mineralogical and isotopic characteristics can be best understood in the context of formation of Mesquite by condensation and isotopic fractionation associated with this process. Once the inclusion formed, it was never molten. However, the Mesquite's rounded to polygonal shape, coarser-grained core melilite (compared to that in the rim) and the lack of a nodular substructure are more consistent with the "compact" type A (CTA) lithology, which is normally interpreted as having crystallized from a melt (e.g., MacPherson and Grossman, 1984; Simon et al., 1999).

4.1.1. The nebular history of Mesquite based on Al-Mg systematics and oxygen isotope ratios

One way to reconcile the seemingly conflicting scenarios would be condensation and coagulation of minerals to form

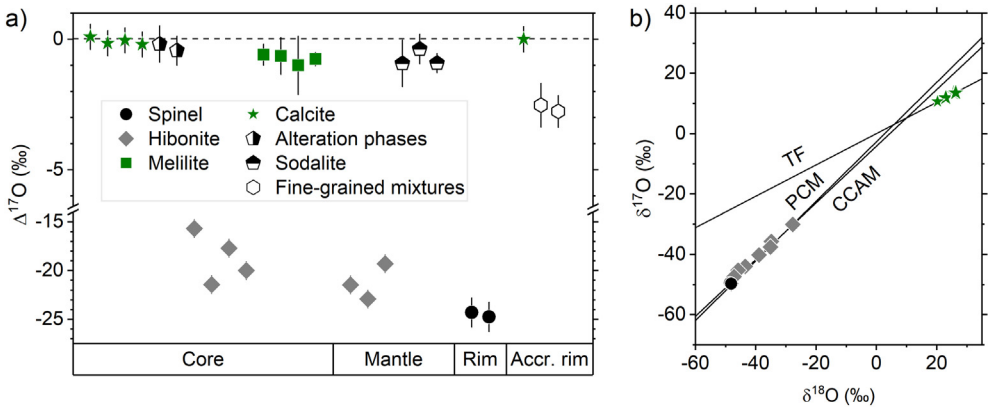

Fig. 7. Oxygen isotope systematics of minerals in Mesquite. (a) Spinel and hibonite plot close to the CCAM (Clayton et al., 1977) or PCM (Ushikubo et al., 2012) lines in the oxygen three-isotope diagram. Calcite is ^{16}O-poor and plots on the TF line. (b) The $\Delta^{17}O$ values of calcite are similar to those of the alteration products associated with the hibonite domains in the core and that of the accretionary rim. Melilite is slightly more ^{16}O-rich.

Table 3
Oxygen isotope ratios of phases in Mesquite.

Analysis	Mineral	Textural position	$\delta^{17}O$	2SD[a]	$\delta^{18}O$	2SD[a]	$\Delta^{17}O$	2SD[b]
O3-IV-Cal-1	Calcite	Core	13.43	0.76	25.66	1.23	0.09	0.49
O3-IV-Cal-2	Calcite	Core	11.84	0.76	23.07	1.23	−0.16	0.49
O3-IV-Cal-3	Calcite	Core	13.55	0.76	26.15	1.23	−0.04	0.49
O3-IV-Cal-4	Calcite	Core	13.52	0.76	26.38	1.23	−0.20	0.49
O3-IV-Alter-1	Phyll + Calcite	Core					−0.19	0.71
O3-IV-Alter-2	Phyll + Calcite	Core					−0.44	0.55
O3-III-Hib-1	Hibonite	Core	−30.10	0.35	−27.71	0.82	−15.69	0.26
O3-III-Hib-2	Hibonite	Core	−44.03	0.35	−43.43	0.82	−21.45	0.26
O3-III-Hib-3	Hibonite	Core	−35.78	0.35	−34.77	0.82	−17.70	0.26
O3-III-Hib-4	Hibonite	Core	−40.21	0.35	−38.89	0.82	−19.99	0.26
O3-III-Mel-1	Melilite	Core					−0.60	0.40
O3-III-Mel-2	Melilite	Core					−0.64	0.71
O3-IV-Mel-3	Melilite	Core					−1.00	1.12
O3-IV-Mel-4	Melilite	Core					−0.77	0.26
O3-III-Hib-5	Hibonite	Mantle	−45.31	0.35	−45.83	0.82	−21.48	0.26
O3-III-Hib-6	Hibonite	Mantle	−47.41	0.35	−47.13	0.82	−22.90	0.26
O3-III-Hib-7	Hibonite	Mantle	−37.55	0.35	−35.11	0.82	−19.29	0.26
O3-IV-Sod-1	Sodalite	Mantle					−0.93	0.89
O3-IV-Sod-2	Sodalite	Mantle					−0.38	0.57
O3-IV-Sod-3	Sodalite	Mantle					−0.92	0.37
O3-I-Sp-1	Spinel	Rim	−49.52	0.92	−48.48	1.42	−24.31	1.51
O3-I-Sp-2	Spinel	Rim	−49.77	0.92	−48.09	1.42	−24.76	1.51
O3-IV-Cal-5	Calcite	Accr. rim	10.56	0.76	20.32	1.23	−0.01	0.49
O3-IV-Mix-1	Fe-rich oxides	Accr. rim					−2.53	0.84
O3-IV-MIx-2	Fe-rich oxides	Accr. rim					−2.77	0.61

[a] External reproducibility on standards.
[b] External reproducibility on standards or in-run variation (2SE).

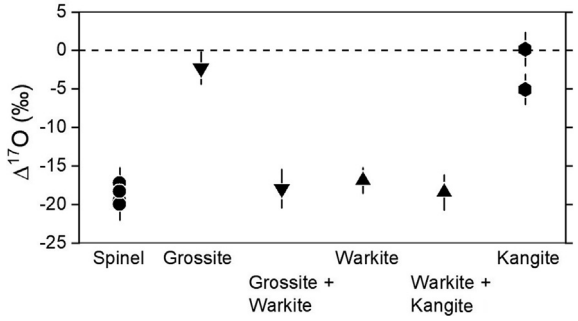

Fig. 8. Graph showing oxygen isotopic composition of minerals in Y24. Spinel and warkite are ^{16}O-rich, whereas the two grossite analyses show either ^{16}O-rich or -poor compositions.

Mesquite. After condensation of hibonite and melilite in the core and subsequent formation of the mantle and rim layers, Mesquite could have undergone heating at subsolidus temperatures (melilite, $T < 1400$ K, Stolper, 1982), which turned the inclusion into a hot plastic solid, followed by slow cooling to allow for solid-state recrystallization (sintering) and coarsening of melilite in the core. A similar texture of melilite has been reported for a synthetic refractory inclusion that recrystallized after being heated to a subsolidus temperature (Fig. 2b of Mendybaev et al., 2006). Spinel and hibonite both have higher melting temperatures (e.g., > 1773 K; Beckett and Stolper, 1994) than melilite so they would have been unaffected by such thermal processing.

The interpretation that Mesquite was never molten (with perhaps the exception of the outermost rim) is supported by its Al-Mg systematics. This inclusion, regardless of the phase, is generally characterized by slightly negative, yet somewhat homogeneous, $\delta^{25}Mg$ of -7 ± 3‰/amu, except for spinel in the outermost rim (which has $0‰ \leq \delta^{25}Mg \leq 3‰$, and will be discussed briefly later) and one melilite analyzed in the mantle layer. Further, Mesquite has a well-constrained ^{26}Al isochron, the slope and intercept of which correspond to $^{26}Al/^{27}Al = (4.95 \pm 0.08) \times 10^{-5}$ and $\delta^{26}Mg^*_0 = -0.14 \pm 0.05‰$, respectively. This suggests that Mesquite derived its observed magnesium isotopic composition from gas-solid condensation, instead of crystallization from a completely molten precursor. There are two arguments in favor of this interpretation. First, complete melting often is accompanied by isotopic homogenization, and to some extent, evaporative loss of and isotopic fractionation of relatively volatile components, such as Mg (e.g., Richter et al., 2007). If the inclusion was molten at low (nebular) pressures, Mg would have evaporated and undergone Rayleigh fractionation, leaving isotopically heavy Mg in the inclusion (e.g., Grossman et al., 2000, 2008). Type B CAIs found in CV3 chondrites, which are thought to have been at least partially molten (e.g., Stolper, 1982; MacPherson and Grossman, 1984; Stolper and Paque, 1986) and commonly show positive magnesium isotope fractionations, are best understood in this context (e.g., Richter et al., 2002). The second reason is that if Mesquite was once molten, its $^{26}Al/^{27}Al$ ratio would have marked the timing of recrystallization, which is 5×10^4 yr

Table 4
Oxygen isotope ratios of minerals in inclusion Y24.

Analysis	Mineral	$\delta^{17}O$	2SD[a]	$\delta^{18}O$	2SD[a]	$\Delta^{17}O$	2SD[b]
O3-II-Sp-1	Spinel	−41.90	2.08	−47.43	3.11	−17.24	2.04
O3-II-Sp-2	Spinel	−43.17	2.08	−45.54	3.11	−19.48	2.04
O3-II-Sp-3	Spinel	−41.89	2.08	−42.11	3.11	−20.00	2.04
O3-II-Sp-4	Spinel	−42.78	2.08	−47.09	3.11	−18.30	2.04
O3-II-War-1	Warkite					−16.90	1.66
O3-II-War-2	Warkite + kangite					−18.45	2.29
O3-II-Ka-1	Kangite					−5.07	1.96
O3-II-Ka-2	Kangite					0.13	2.17
O3-II-Grs-1	Grossite					−2.31	2.11
O3-II-Grs-2	Grossite + warkite					−17.95	2.53

[a] External reproducibility on standards.
[b] External reproducibility on standards or in-run variation (2SE).

Table 5
Al-Mg systematics of Mesquite.

Analysis	Mineral	Domain	$^{27}Al/^{24}Mg$	2SE	$\delta^{26}Mg^*$	2SE	$\delta^{25}Mg$	2SE
FCII_Hib@4	Hibonite	Core	26.90	1.40	9.10	0.49	−7.52	0.28
FCII_Hib@3	Hibonite	Core	29.61	1.57	10.22	0.41	−7.35	0.20
FCII_Hib@2	Hibonite	Core	23.29	1.18	8.41	0.52	−7.60	0.37
FCII_Hib@1	Hibonite	Core	23.26	1.16	8.07	0.48	−6.74	0.22
EMII_Mel@1	Melilite	Core	53.53	0.56	16.56	3.45	−5.23	2.14
EMII_Mel@2	Melilite	Core	172.57	1.93	66.01	5.00	−12.78	2.51
EMII_Mel@3	Melilite	Core	63.21	0.66	22.70	3.59	−6.48	2.16
EMII_Mel@4	Melilite	Core	68.21	0.71	23.57	3.09	−6.17	2.06
EMII_Mel@5	Melilite	Core	66.36	0.69	25.06	2.60	−7.42	1.55
EMII_Mel@11	Melilite	Core	342.13	3.75	118.40	7.94	−2.67	3.92
EMII_Mel@12	Melilite	Core	33.17	0.34	10.14	2.77	−7.16	1.32
EMII_Mel@13	Melilite	Core	31.81	0.33	12.61	2.37	−7.31	1.28
EMII_Mel@14	Melilite	Core	94.00	0.99	36.99	3.30	−6.93	2.04
FCI_Hib@2	Hibonite	Mantle	41.82	0.58	14.05	0.47	−6.88	0.23
FCI_Hib@3	Hibonite	Mantle	29.06	0.40	10.86	0.54	−7.37	0.29
FCI_Hib@4	Hibonite	Mantle	21.09	0.29	7.50	0.37	−6.47	0.20
FCI_Hib@5	Hibonite	Mantle	45.98	0.64	15.74	0.78	−7.49	0.41
FCI_Hib@6	Hibonite	Mantle	29.94	0.41	11.71	0.55	−7.11	0.27
FCI_Hib@7	Hibonite	Mantle	29.05	0.43	10.31	0.49	−6.24	0.28
FCI_Hib@8	Hibonite	Mantle	32.43	0.45	10.66	0.70	−6.18	0.34
FCI_Hib@9	Hibonite	Mantle	23.73	0.35	8.32	0.43	−2.65	0.22
FCI_Hib@10	Hibonite	Mantle	27.60	0.38	9.26	0.37	−7.34	0.18
EMII_Mel@6	Melilite	Mantle	203.29	2.29	74.63	5.90	−5.19	3.48
EMII_Mel@7	Melilite	Mantle	94.83	1.74	30.43	3.42	−6.01	2.34
EMII_Mel@8	Melilite	Mantle	183.69	1.98	66.60	6.22	−4.96	3.72
EMII_Mel@9	Melilite	Mantle	61.75	0.69	20.12	3.26	−4.33	1.63
EMII_Mel@10	Melilite	Mantle	50.59	0.56	19.30	4.03	1.50	2.63
FCI_Sp@1	Spinel	Mantle	2.63	0.03	0.57	0.24	−2.88	0.21
FCI_Sp@2	Spinel	Mantle	2.68	0.03	0.84	0.23	−3.68	0.20
FCI_Sp@3	Spinel	Rim	2.68	0.03	0.81	0.10	3.26	0.17
FCIII_Sp@1	Spinel	Rim	2.82	0.07	0.83	0.12	0.02	0.16
FCIII_Sp@2	Spinel	Rim	2.76	0.07	0.71	0.12	−0.05	0.17
FCIII_Sp@3	Spinel	Rim	2.77	0.07	0.92	0.10	1.31	0.16
FCIII_Sp@4	Spinel	Rim	2.84	0.07	0.90	0.12	0.27	0.17
FCIII_Sp@5	Spinel	Rim	2.76	0.07	0.84	0.13	0.97	0.17

after the large CV CAIs in CV chondrites formed at $^{26}Al/^{27}Al = 5.2 \times 10^{-5}$ (e.g., Jacobsen et al., 2008), or $\sim 10^5$ yr after dust condensation and coagulation started, with $^{26}Al/^{27}Al = 5.4 \times 10^{-5}$ (Liu et al., 2019). However, given the high bulk $^{27}Al/^{24}Mg$ ratio of Mesquite ($\sim$15), to arrive at the current intercept value of $\delta^{26}Mg^*_0 = -0.14‰$ at the time of recrystallization, the starting (pre-^{26}Al decay) $\delta^{26}Mg^*_0$ value of Mesquite's precursor materials would have been –0.42‰ or –0.64‰, depending on the reference time point chosen ($^{26}Al/^{27}Al = 5.2 \times 10^{-5}$ or 5.4×10^{-5}, respectively). Even though literature data suggest that $\delta^{26}Mg^*_0$ in the CAI formation reservoir(s) appeared to be slightly heterogeneous when $^{26}Al/^{27}Al$ was uniform at 5.2 ($\pm$0.1) $\times 10^{-5}$ (e.g., Larsen et al., 2011; Wasserburg et al.,

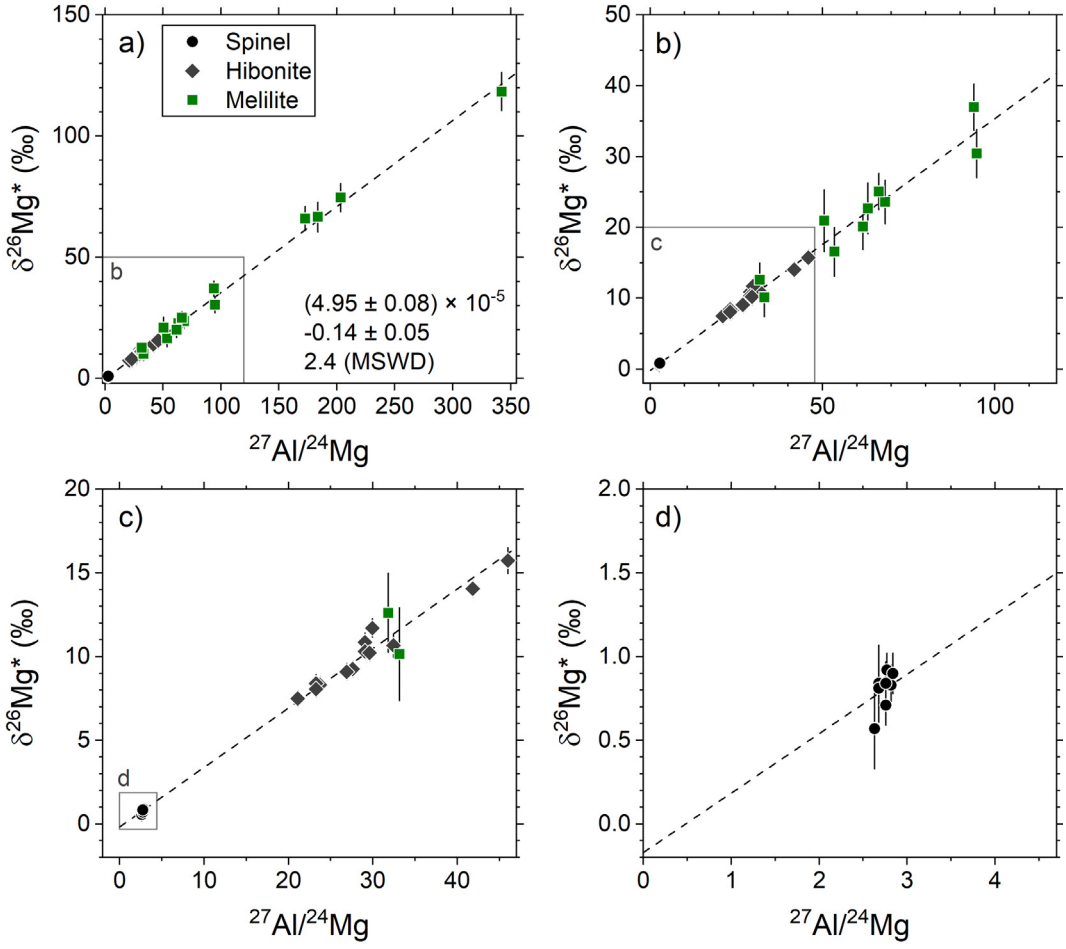

Fig. 9. (a) Isochron diagram of Mesquite and (b-d) diagrams showing zoomed-in sections of the same dataset shown in (a). All analyses plot on a single isochron regardless of the textural position of analyzed minerals. Uncertainties on slope and intercept are 95%-confidence intervals; uncertainties of individual analyses are on the 2σ level.

2012; MacPherson et al., 2017; Larsen et al., 2020), both –0.42‰ and –0.64‰ far exceed the range (from –0.13 to –0.014‰ relative to a terrestrial reference value) reported for CAIs carrying the canonical ^{26}Al abundance. Therefore, we argue that the magnesium isotopic composition of all the phases of Mesquite must have evolved by closed-system behavior (i.e., never disturbed) since the formation of this inclusion by condensation, which took place when $^{26}Al/^{27}Al = (4.95 \pm 0.08) \times 10^{-5}$.

Spinel in the outermost rim, albeit plotting on the same ^{26}Al isochron as the mantle and core hibonite and melilite, shows heavier δ^{25}Mg values ($0‰ \leq \delta^{25}Mg \leq 3‰$) compared to them. Normally, positive δ^{25}Mg is understood to be a result of isotope fractionation associated with evaporation of a molten droplet, which tends to enrich the residues in heavy relative to light isotopes. Therefore, the outermost rim of Mesquite could have been melted by flash heating and then cooled not too long after final coagulation so that spinel still records the same ^{26}Al abundance as the rest of the inclusion. As will be discussed later, for this scenario to be consistent with the observed oxygen isotopic compositions, the surrounding gas during remelting of the outermost rim must have been ^{16}O-rich (with $\Delta^{17}O = -25‰$), otherwise exchange between a melt and the gas would have resulted in rapid isotopic equilibration and erased the original oxygen isotopic composition of the spinel. For example, at a temperature at which spinel could melt (e.g., 1773 K; diffusivity taken from Ryerson and McKeegan, 1994), it would take no more than a couple of seconds to homogenize oxygen isotopes in a 20 μm-thick molten layer. An alternative explanation for spinel's relatively isotopically heavy δ^{25}Mg but ^{16}O-rich oxygen isotope composition would be that this mineral phase in the rim condensed from an ^{16}O-rich gas reservoir with an already fractionated magnesium isotopic composition, which could potentially be realized if lighter magnesium isotopes have been depleted by kinetic condensation of interior phases of Mesquite. If this scenario is correct, the formation of Mesquite must have proceeded very quickly so that the gas parcel in which Mesquite formed would have remained isotopically heavy (in magnesium) at the late stages of condensation.

4.1.2. Implications for the formation of first solids in the early Solar System

The combination of inferred ^{26}Al abundance and initial $\delta^{26}Mg_0$* value of Mesquite also has an important implica-

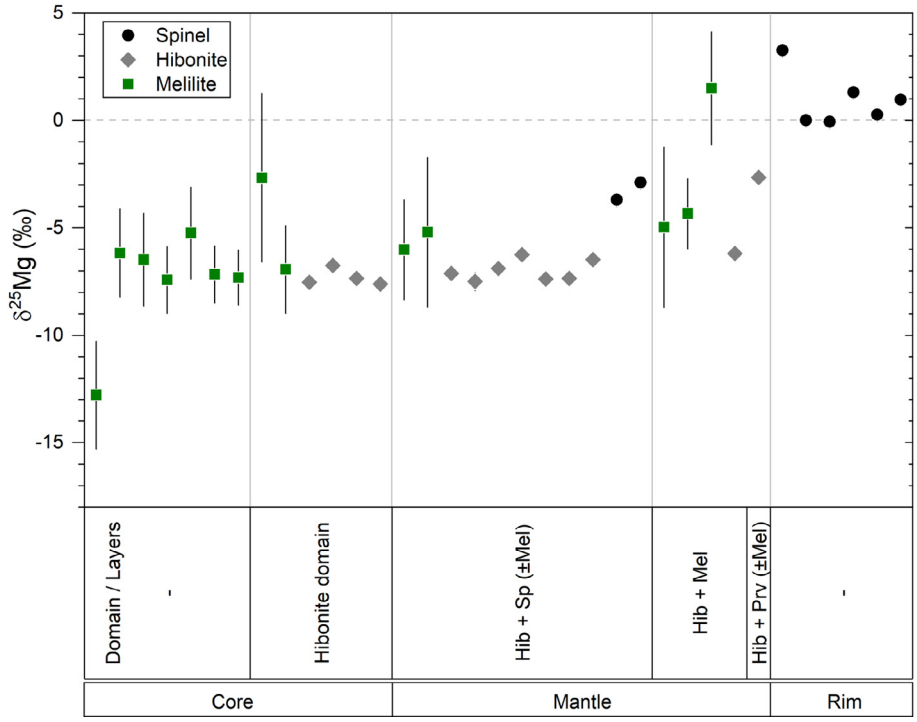

Fig. 10. Graph showing δ^{25}Mg values of minerals from different layers or domains of Mesquite. Except for spinel of the rim and one melilite in the mantle, Mg isotopes are negatively fractionated. Uncertainties of individual analyses are on the 2σ level.

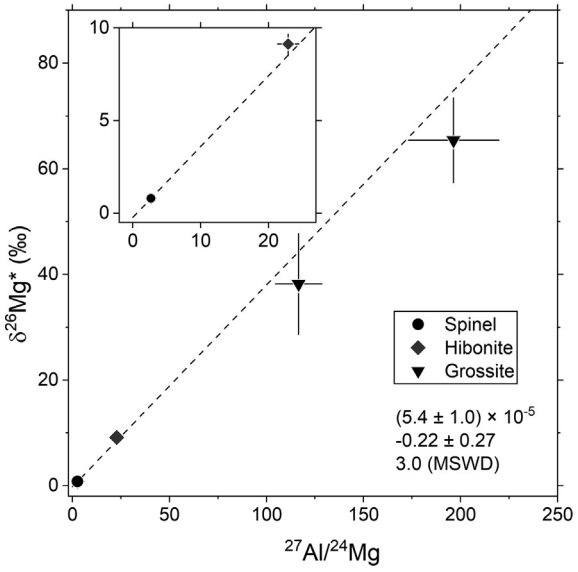

Fig. 11. Isochron diagram of minerals in Y24. Uncertainties on slope and intercept are 95%-confidence intervals; uncertainties of individual analyses are on the 2σ level.

tion for formation of solids in the early Solar System. Through in-situ analysis of ~two dozen very small (~30–100 μm) CAIs from one of the most primitive CO3 chondrites, Allan Hills 77307, Liu et al. (2019) showed that most of the samples formed two major populations with regard to inferred $^{26}Al/^{27}Al$ and $\delta^{26}Mg_0$*: one group appears to have formed earlier, with $^{26}Al/^{27}Al = 5.4 \times 10^{-5}$ (marking the timing of dust condensation and coagulation) and initial $\delta^{26}Mg_0^* = -0.14‰$, whereas the other registers slightly lower $^{26}Al/^{27}Al = 4.9 \times 10^{-5}$ and elevated $\delta^{26}Mg_0^* = -0.04‰$. Although such a relationship between $^{26}Al/^{27}Al$ and $\delta^{26}Mg_0$* was interpreted as a result of reprocessing of earlier-formed inclusions by a nebula-wide thermal event when $^{26}Al/^{27}Al = 4.9 \times 10^{-5}$, it may also be compatible with a scenario of formation of another generation of CAIs in a slightly Mg-heterogeneous gas (Liu et al., 2019). As stated previously, high-precision bulk and in-situ magnesium isotope data available to date suggest that the CAI formation reservoir(s), albeit with homogeneous $^{26}Al/^{27}Al$ of 5.2×10^{-5}, were characterized by an apparent $\delta^{26}Mg_0$* heterogeneity, with values between –0.13 to –0.014‰ (e.g., Larsen et al., 2011; Wasserburg et al., 2012; MacPherson et al., 2017). If this Mg heterogeneity in the gas had persisted to $^{26}Al/^{27}Al = 4.9 \times 10^{-5}$, the increase in $\delta^{26}Mg_0$* due to the decay of $^{26}Al/^{27}Al$ from 5.2×10^{-5} would have only been 0.002‰ (or 0.004‰ if from 5.4×10^{-5}) in a gas reservoir of solar composition ($^{27}Al/^{24}Mg = 0.101$, Lodders, 2003). As a condensate, Mesquite's $\delta^{26}Mg_0$* of $-0.14 \pm 0.05‰$ implies that this value would have also characterized the gas reservoir in which this inclusion formed. The meaning of this inference is twofold. (1) A thermal event that had disturbed some of the earlier-formed inclusions could have also led to formation of new inclusions. Therefore, there could have been multiple generations of CAIs forming in the solar nebula, a conclusion similar to what other studies of fine-grained CAIs from pristine chondrites (COs and reduced CV3) have suggested (e.g., Ushikubo et al., 2017; Kawasaki et al., 2020). (2)

Table 6
Al-Mg systematics of Y24.

Analysis	Mineral	$^{27}Al/^{24}Mg$	2SE	$\delta^{26}Mg^*$	2SE	$\delta^{25}Mg$	2SE
FCII_Y24_Hib@1	Hibonite	22.90	1.57	9.13	0.54	−2.26	0.25
FCII_Y24_Sp@4	Spinel	2.68	0.11	0.81	0.09	0.10	0.12
EMI_Y24_Gros@3	Grossite	196.42	23.36	65.40	8.03		
EMI_Y24_Gros@4	Grossite	116.53	11.98	38.22	9.56		

Magnesium isotopes (more specifically, $\delta^{26}Mg_0^*$) may have continued to have been somewhat heterogeneous in the gas even when $^{26}Al/^{27}Al = 4.9 \times 10^{-5}$. If the latter is true, it may pose a challenge for the dynamic modeling of isotope mixing in the solar nebula.

4.1.3. Variable $\Delta^{17}O$ values of hibonite in core and mantle: ^{16}O-rich gas with shifting oxygen isotopic compositions

In contrast to the undisturbed magnesium isotopes, the oxygen isotopic compositions in Mesquite may have been affected by some level of open-system isotopic exchange. Spinel in the rim is characterized by uniform ($\delta^{17}O$, $\delta^{18}O$) = (~–49.5‰, ~–48.3‰) or $\Delta^{17}O$ of ~–25‰, which is very typical of this mineral in CAIs (e.g., Ireland et al., 2020). Hibonite in the core and mantle is less enriched in ^{16}O relative to spinel, with $\Delta^{17}O$ ranging from –16‰ to –23‰, and the core on average appears more ^{16}O-poor than the mantle, despite the fact that only a handful of points in each domain exist. It should be pointed out that various degrees of "contamination" with secondary phases appeared in the majority of the analyzed spots (shown in EA1). Although contamination with secondary phases would certainly have affected the $\Delta^{17}O$ values of hibonite, they were unlikely to account for the full range of the variation. The oxygen isotopic compositions in melilite appear to be more ^{16}O-depleted compared to those in spinel and hibonite, but we will show later that such isotopic characteristics were possibly derived from thermal reprocessing of melilite. Given the slow diffusion rates of oxygen isotopes in spinel and hibonite (e.g., $\sim 10^{-22}$ and $\sim 10^{-23}$ m^2 s^{-1}, respectively, at 1400 K; Ryerson and McKeegan, 1994; Lagerlof et al., 1989; note that the diffusivity of oxygen in hibonite was approximated by using that in MgO-doped sapphire), the observed $\delta^{17}O$ and $\delta^{18}O$ values in the two phases most likely reflect the oxygen isotopic characteristics of the nebular gas from which they condensed. Alternatively, it is still possible that ^{16}O-rich spinel in the rim was melted by flash heating and then crystallized in a still ^{16}O-rich setting, most likely soon after coagulation of Mesquite was finished. Regardless of the scenario, slightly less negative, but variable $\Delta^{17}O$ in the core and mantle hibonite compared to that of rim spinel would imply that Mesquite condensed and coagulated within a timescale of 3.3×10^4 yr (calculated from the isochron error) in an ^{16}O-rich gas with changing oxygen isotopic compositions from $\Delta^{17}O$ ~–18‰ to –25‰. If this interpretation is correct, Mesquite would be one rare example of a CAI (excluding platy hibonite crystals, e.g., Liu et al., 2009; Kööp et al., 2016) that contains hibonite with pristine (nebular), but heterogeneous $\Delta^{17}O$ values (e.g., Krot, 2019).

4.1.4. ^{16}O-poor melilite: Oxygen isotope exchange in the solar nebula or on the parent-body asteroid?

Based on the consistent $\delta^{25}Mg$ values and tight ^{26}Al isochron, core melilite and hibonite must have condensed contemporaneously (within the temporal resolution of ^{26}Al chronometry), and therefore should have very similar, if not identical, enrichments in ^{16}O. However, melilite has the most ^{16}O-poor compositions compared to hibonite and spinel, and its $\Delta^{17}O$ values cluster around –1‰. This result suggests that melilite underwent isotope exchange with an ^{16}O-poor component. Since the magnesium isotopic composition of Mesquite suggests that this inclusion has either never been melted or experienced very limited melting in the outermost rim, isotope exchange via solid-state diffusion would be the most feasible explanation. For melilite to have retained pristine magnesium but lost the original oxygen isotopic compositions, the maximum temperature Mesquite experienced must not have exceeded 1493 K, which is consistent with the sub-solidus temperature of melilite, so that magnesium would be a slower diffuser than oxygen in melilite (see Yurimoto et al., 1989; Ryerson and McKeegan, 1994; Ito and Ganguly, 2009). If isotope exchange with the nebular gas was responsible for the altered oxygen isotopic composition of melilite, heating of the inclusion to no more than 1493 K must have taken place when it was surrounded by a ^{16}O-poor gas; the timing of this thermal event, however, did not affect the inclusion's magnesium isotopes or ^{26}Al isochron.

Judging from the low petrologic subtype of NWA 7892 (3.05, The Meteoritical Bulletin, No. 102), which indicates low peak temperatures (<700 K; Schwinger et al., 2016; Imae and Nakamuta, 2018) of parent body metamorphism, melilite was unlikely to have exchanged its oxygen isotopes with an ^{16}O-poor fluid in the meteorite parent body. Complete isotope equilibration between an ^{16}O-poor fluid and a 100-μm melilite crystal by thermally driven solid-state diffusion of oxygen would take longer than any reasonable residence time of liquid water in chondrite parent bodies (e.g., 9 million years for CI chondrites; Fujiya et al., 2013); however, diffusion rates of oxygen in silicates under wet conditions, relative to dry conditions (Farver, 2010, and references therein), are known to be much faster. This could have significantly shortened the required timescales for equilibration and opens up the possibility of fluid-enhanced oxygen isotope exchange and alteration of the originally ^{16}O-rich melilite. Further, parent body processes have been commonly suggested to be the main cause of the relatively ^{16}O-poor and variable oxygen isotope compositions of melilite in CAIs from carbonaceous chondrites of petrologic subtypes ≥3.1 (e.g., Wasson et al., 2001; Itoh et al., 2004; Zhang et al., 2020).

A recent oxygen isotope study of a smaller CAI (~100 μm) from NWA 7892, however, found $\delta^{17}O$ and $\delta^{18}O$ values of ~−50‰ for both spinel and melilite (Zhang et al., 2020), suggesting that the effects of asteroidal fluids likely were minimal in the studied thin section of NWA 7892. While alteration of the oxygen isotope composition of melilite on the parent body cannot be ruled out, we suggest that the melilite in Mesquite obtained its oxygen isotope composition by exchange with an ^{16}O-poor gas in the Solar nebula, based on the low petrologic subtype of NWA 7892 and the presence of ^{16}O-rich melilite in a different CAI from the same meteorite (Zhang et al., 2020).

4.1.5. Alteration products in Mesquite: terrestrial or asteroidal?

There is abundant evidence for low-temperature alteration throughout Mesquite. This includes calcite, mineralogically uncharacterized phyllosilicates and sodalite that fill veins and voids in the core, mantle layers, and rim. Further, the brownish portion of Mesquite, which roughly traces the outline of mantle layers as seen in the optical photomicrograph (Fig. 1a), corresponds to elevated Ni and Fe contents in EDS X-ray maps, indicating some degree of oxidation by a fluid.

The occurrence of these secondary phases begs a question about their origins. Core and rim calcite and core phyllosilicates all have $\Delta^{17}O = 0‰$. Although this value falls in the range of $\Delta^{17}O$ for meteoritic calcite grains from CM chondrites (~−2 to 2‰; e.g., Fujiya et al., 2015), the lack of variation is more consistent with precipitation from terrestrial water introduced during the weathering process on the Earth's surface. In contrast, sodalite measured here on average is characterized by a $\Delta^{17}O$ value close to −1‰. Given that sodalite formation requires a Cl-rich fluid to transport Na into primary phases to replace Ca and Mg, this $\Delta^{17}O$ value most likely is derived from the original mineral, which was ^{16}O-rich, being altered by isotopically heavy water. When and where this alteration process took place is not well-constrained. Water in the parent-body asteroid remains a possibility, but transformation of the primary phase into sodalite by terrestrial weathering cannot be ruled out, especially when there is already evidence for terrestrial water flowing through the inclusion. However, if sodalite indeed formed on the parent body, it would indicate high water-to-rock ratios and provide strong evidence for fluid-driven and -enhanced oxygen isotope exchange of melilite in an asteroidal setting. To shed light on this question, analysis of sulfur isotopes in sodalite seeking the fossil record of another short-lived radionuclide ^{36}Cl ($t_{1/2} = 0.3$ Myr) would be necessary (see e.g., Lin et al., 2005; Hsu et al., 2006; Tang et al., 2017).

4.2. Inclusion Y24 – The largest isolated UR inclusion known to date

Previous REE measurements of several CAIs with abundant Zr- and Sc-rich phases all yielded ultrarefractory REE patterns; hence, it is suggested that inclusions rich in these rare minerals can be classified as UR inclusion even though no REE patterns have been obtained (Krot, 2019, and references therein). This could certainly be the case for the warkite- and kangite-rich CAI Y24. A recent and comprehensive study on UR inclusions by Krot et al. (2019a) listed 34 samples that have been found prior to our study, of which 20 are isolated objects in the matrix like Y24. The largest of these isolated UR inclusions measures 120 μm in its longest dimension, but stills pales in comparison to Y24 (max. 300 μm). Of the seven described CO chondrite UR inclusions (isolated + compound objects), none contains grossite, and only one is free of silicates like Y24.

4.2.1. The nebular history of Y24

The negatively fractionated $\delta^{25}Mg$ in hibonite (Table 6) and the irregular shape of Y24 point to a condensation origin and suggest that Y24 was never molten. However, there is petrographic evidence that Y24 represents more than a simple aggregate of once separate condensate grains. Almost every grossite lath has anhedral spinel that is located close to its edge and is interpreted to have formed by replacement of grossite. Accordingly, the aggregate of spinel grains in the lower left of Y24 in Fig. 4a could have formed by complete pseudomorphic replacement of grossite. Grossite, in turn, could have formed even earlier by reaction between hibonite and the nebular gas, as expected for equilibrium condensation (e.g., Fegley, 1982; Grossman, 2010). However, the only hibonite lath in Y24 shares a straight grain boundary with adjacent spinel, suggesting that no such reaction took place between both minerals.

Simon et al. (2019a) described a grossite-bearing inclusion (31-2) from DOM 08006 that shares some textural similarities with Y24. The inclusion 31-2 records an almost complete condensation sequence: hibonite in the core is surrounded by grossite + perovskite, which in turn is surrounded by melilite. Some spinel grains are in between the grossite and melilite layers. Texturally, spinel formed earlier than melilite, although the reverse would be expected from a gradually cooling gas. Importantly, as in Y24, spinel in 31-2 does not form a continuous rim around grossite but occurs as isolated and elongated patches at the edges of grossite. The main difference between inclusions Y24 and 31-2, however, is the presence of the silicates melilite and diopside in the latter that are completely absent in Y24. Given that Y24 inclusion is essentially Si-free, it must have largely condensed above the condensation temperature of melilite, and its mineralogy appears to be consistent with the condensation sequence of corundum (although completely replaced) followed by hibonite, grossite, and spinel (e.g., Fegley, 1982; Grossman, 2010). This inference is supported by the petrographic observation that spinel partially replaced grossite in Y24.

Inclusion Y24 is warkite-rich and shows faint mineralogical zoning: the center is dominated by refractory-element-rich oxides, whereas grossite laths are located towards the edge of the inclusion (Fig. 4). Oxides and grossite laths are themselves embedded in a matrix made of warkite ($Ca_2Sc_6Al_6O_{20}$), which is therefore texturally late. Warkite, grossite, and hibonite could, however, have formed nearly simultaneously after the refractory oxides

or their precursor phases had started to condense. If warkite grew faster than grossite and hibonite, it would have enclosed both minerals during its growth; this would also explain the observed textural relationship.

Thermodynamic data are not yet available for warkite, so this phase does not appear in calculations of equilibrium condensation sequences. Fortunately, the thermodynamic properties of the CaO-Al_2O_3-Sc_2O_3 system are of interest to material scientists because knowledge of these properties help define process parameters for the recovery of rare-earth and other trace elements from metallurgical slags. The first assessment of this ternary system was recently undertaken by Zhi et al. (2019). These authors performed quench experiments in an Ar atmosphere and constructed isothermal sections of the phase relationships at 1773 K and 1873 K. Isothermal sections show $Ca_2Sc_6Al_6O_{20}$ as the liquidus phase for Sc-rich starting compositions as well as a three-phase region at Al-rich bulk compositions comprising CA_2 ($CaO{\cdot}2Al_2O_3$), CA_6 ($CaO{\cdot}6Al_2O_3$), and $Ca_2Sc_6Al_6O_{20}$ (Zhi et al., 2019), which correspond stoichiometrically to the minerals grossite, hibonite, and warkite, respectively. Although the study did not specify crystallographic information such as space group and cell parameters for these three phases, it did characterize the cell parameters of the phase CA ($CaO{\cdot}Al_2O_3$), which occurs at lower Al contents. Results for CA are in agreement with krotite (Ma et al., 2011). It should be pointed out that the phase relationships obtained by melting experiments may not be directly applicable to condensates (grossite and warkite), but experiments such as those carried out by Zhi et al. (2019) still offer general insights into the expected phase relationships during condensation and show that phases with chemical compositions similar to those of grossite, hibonite, and warkite might have formed simultaneously in a cooling gas.

4.2.2. Heterogeneous oxygen isotopic composition of Y24

Spinel and warkite in Y24 are ^{16}O-rich ($\Delta^{17}O \sim -17$‰ to -20‰) whereas kangite and grossite are characterized by ^{16}O-poor compositions ($-5‰ < \Delta^{17}O < 0‰$). Ivanova et al. (2012) measured the oxygen isotopic compositions of Zr-,Sc-,Y-rich oxides in two compound CAIs from CV chondrites that contain UR inclusions and found these oxides to be depleted in ^{16}O ($\Delta^{17}O \sim -5‰$ to $-2‰$) relative to spinel. Based on petrographic observations, the authors concluded that one of the inclusions experienced melting and Zr-, Sc-, Y-rich oxides likely exchanged oxygen isotopes with an ^{16}O-poor gas. Further, Krot (2019) offered an extensive dataset on oxygen isotopes of UR inclusions and compiled oxygen isotope data of grossite-bearing inclusions (Simon et al., 2019a, 2019b; Krot et al., 2019b) in unaltered and metamorphosed carbonaceous chondrites. UR inclusions found in CO3.0 chondrites are ^{16}O-rich with very limited spread ($-25‰ \leq \Delta^{17}O \leq -20‰$), regardless of the phases (hibonite, melilite, grossite, warkite, etc.). In contrast, UR inclusions and grossite-bearing inclusions found in CO chondrites of petrologic type ≥ 3.1 show heterogeneous, mineralogically-dependent oxygen isotope compositions, with a trend of decreasing degree of ^{16}O enrichment from spinel ($\Delta^{17}O = -24 \sim -26‰$), certain Zr-,Sc-,Y-rich oxides (e.g., warkite and davisite ($CaScAlSiO_6$), $\Delta^{17}O = -23 \sim -2‰$) and kangite ($\Delta^{17}O = -2‰$; only a handful of data points due to the extremely rare occurrence). The oxygen isotope heterogeneities in UR CAIs from CO chondrites of such petrologic types have been interpreted to result from exchange with fluids on the parent bodies (Krot et al., 2019a). Yamato 81020 is a CO 3.05. The implication of this observation is that if ^{16}O-poor asteroidal water, with an inferred $\Delta^{17}O$ of $-0.3 \pm 0.7‰$ (Doyle et al., 2015) was responsible for the observed oxygen isotope variation in Y24, as suggested for CO3.1 chondrites by Krot et al. (2019b) and Simon et al. (2019b), water–rock interactions disturbing the CAIs' oxygen isotopes could have started in CO chondrites with a petrologic type as low as 3.05. However, such effects may have been local and limited, as other refractory inclusions from this chondrite have isotopically uniform $\Delta^{17}O$ of $-23‰$ (e.g., Ushikubo et al., 2017). In this context Krot et al. (2019b) described grossite, in an inclusion from Y-81020, that is ^{16}O-depleted to various degrees, probably due to fluid-assisted thermal metamorphism.

Alternatives to isotope exchange inside the parent bodies include condensation of Y24 in a gas of variable oxygen isotopic composition (similar to that proposed in e.g., Park et al., 2012) and isotope exchange with an ^{16}O-poor gas in a nebular setting. The total variation, which appears to be somewhat bimodal (at $\Delta^{17}O = -20‰$ and $\sim 0‰$), is unlikely to be a result of condensation of Y24 taking place in an oxygen-isotopically heterogeneous gas reservoir because one would expect a more random distribution of $\Delta^{17}O$ in Y24. In the context of isotope exchange with an ^{16}O-poor gas component, the interaction between a melt and a gas can be confidently ruled out since Y24 does not show evidence for melting. However, given our ignorance of oxygen diffusivities in warkite, kangite and grossite, solid-state diffusive exchange with the nebular gas still remains plausible for Y24. If this inference is correct, it would imply that oxygen diffuses faster in grossite and kangite than in warkite, despite them all being refractory phases.

4.2.3. First ^{26}Al age on an isolated UR inclusion

This study, for the first time, presents data on the Al-Mg systematics of an isolated UR inclusion. So far, the Al-Mg systematics have only been reported for two UR inclusions that are part of the composite CAIs previously studied by Ivanova et al. (2012). A conference abstract (Park et al., 2014) about these inclusions cited values for $(^{26}Al/^{27}Al)_0$ that are, within uncertainties, indistinguishable from the "canonical" value of $\sim 5.2 \times 10^{-5}$. One of the first attempts to measure Al-Mg systematics in a complex inclusion containing abundant UR oxides showed the presence of ^{26}Al at the time this CAI formed but isochrons are disturbed (El Goresy et al., 2002). A few isolated grossite-bearing CAIs (not UR inclusions) from DOM 08004 and 08006 (CO3.1 and 3.0, respectively) have also been analyzed for ^{26}Al abundances, and three populations of inclusions with regard to the inferred $^{26}Al/^{27}Al$ ratios were identified: 4.5×10^{-5}, 1×10^{-5} and $\ll 10^{-6}$ (Simon et al., 2019b). Further, Makide et al. (2009) studied Al-Mg systematics of grossite-rich CAIs from CR2 chondrites and deduced

model isochrons based on grossite analyses that result in $(^{26}Al/^{27}Al)_0$ of $\sim 4.3 \times 10^{-5}$.

The slightly negative $\delta^{25}Mg$ values found in hibonite provide another line of evidence for Y24 being a condensate inclusion, rather than a recrystallized solid from a melt. Within analytical uncertainty, the three phases plot on a single isochron with $(^{26}Al/^{27}Al)_0 = (5.4 \pm 1.0) \times 10^{-5}$ (MSWD = 3.0, 95%-confidence interval, Fig. 11[1]). The scatter of data around the isochron regression could in part result from the use of inappropriate RSF for grossite, but it does not change the fact that Y24 formed with the presence of ^{26}Al. This initial ratio is indistinguishable from the "canonical" value of $\sim 5.2 \times 10^{-5}$, indicating that the (partial) replacement of grossite by spinel occurred shortly after grossite and hibonite formation, and the process responsible for the ^{16}O-poor composition in grossite had very little effect (if any) on the magnesium isotopic composition. Further, the replacement happened in the same ^{16}O-rich reservoir where most CAIs were formed, as suggested by the oxygen isotopic composition of spinel.

5. CONCLUSIONS

We studied the petrography, oxygen isotopic composition, and Al-Mg systematics of the CAIs Mesquite and Y24 found in the CO3 chondrites NWA 7892 and Y-81020, respectively. Mesquite is unusually large ($\sim 5 \times 3$ mm) for a CAI from a CO chondrite and is mineralogically zoned: a core mostly made of coarse-grained (up to ~ 300 μm) melilite is surrounded by mantle layers [hibonite-spinel(±melilite), hibonite-melilite, hibonite-melilite-perovskite], and a semi-continuous spinel-dominated rim. We envision the following, most likely formation scenario for Mesquite. Based on negatively fractionated $\delta^{25}Mg$ values of melilite, hibonite, and spinel in the mantle layers, it seems likely that the inclusion was never molten as a whole, and its primary phases condensed from the nebular gas. A heating event with a maximum temperature lower than the melilite solidus temperature (1493 K) after initial condensation possibly led to coarsening of melilite in the core by solid-state re-crystallization. All minerals analyzed for their Al-Mg systematics, regardless of their locations within the CAI, plot on a single isochron, the slope and intercept of which corresponds to an $^{26}Al/^{27}Al = (4.95 \pm 0.08) \times 10^{-5}$ and $\delta^{26}Mg^*_0 = -0.14 \pm 0.05$‰. The $^{26}Al/^{27}Al$ ratio is marginally resolved from the "canonical" value and is interpreted to have marked the "formation time", rather than the "reset time", of Mesquite. Together with the $\delta^{26}Mg^*_0$ value, one could infer that condensation of Mesquite took place in a slightly Mg-heterogeneous solar nebula when $^{26}Al/^{27}Al = 4.9 \times 10^{-5}$, which represented the time for a nebula-wide thermal event (Liu et al., 2019), and that there have been multiple generations of CAIs forming in the solar nebula.

Spinel in the rim of Mesquite is ^{16}O-rich ($\Delta^{17}O \sim -25$‰); oxygen isotope ratios of hibonite are also ^{16}O-rich but to a variable degree, and plot along the CCAM line ($\Delta^{17}O \sim -15$‰ to -23‰). Their $\Delta^{17}O$ values are consistent with condensation of Mesquite in an ^{16}O-rich gas with quickly (within the resolution of our ^{26}Al isochron, that is, $\sim 33{,}000$ years) changing $\Delta^{17}O$ from -18‰ to -25‰. Melilite also could have been initially enriched in ^{16}O but later acquired its ^{16}O-poor composition by exchange with an ^{16}O-poor gas during the heating event that also led to coarsening. Since heating did not affect the ^{26}Al isochron, its timing could not be constrained. Alternatively, melilite could have obtained its oxygen isotopic composition by isotopic exchange with an ^{16}O-poor fluid on the parent body. Mesquite shows evidence for extensive low-temperature terrestrial alteration such as formation of calcite and phyllosilicates. Sodalite is present throughout the mantle layers and could have formed by the reaction between a Cl-rich fluid and the primary mineral phases in the parent body.

Inclusion Y24 is a unique, isolated UR inclusion from the CO3.05 chondrite Yamato 81020. Y24 is devoid of silicates and comprises grossite, hibonite, spinel, and ultrarefractory-element-rich oxide phases, such as kangite and warkite, and perovskite. All minerals are embedded in a matrix made of warkite. The irregular shape of the inclusion and the Al-Mg systematics of hibonite indicate that phases are primary condensates. A possible formation scenario for Y24 involves condensation of hibonite, pseudomorphic replacement of it by grossite, and formation of warkite. The textural relationship, i.e. phases embedded in a matrix of warkite, can be explained by relatively fast warkite condensation that outpaced that of grossite and hibonite, or condensation of grossite and hibonite followed by that of warkite. Anhedral spinel patches are located at the edges of grossite laths and are interpreted to have formed at the expense of grossite in a gradually cooling gas, as expected for equilibrium condensation at temperatures above that of melilite stability. The Al-Mg and oxygen isotope systematics of this unique inclusion indicate that hibonite, grossite, and spinel formed in an ^{16}O-rich gas when $^{26}Al/^{27}Al$ was $(5.4 \pm 1.0) \times 10^{-5}$. The ^{16}O-poor compositions of grossite and kangite could have been derived from oxygen isotope exchange with an ^{16}O-poor fluid in the parent body or with an ^{16}O-poor gas by self-diffusion in a nebular setting.

Declaration of Competing Interest

The authors declare that they have no known competing financial interests or personal relationships that could have appeared to influence the work reported in this paper.

ACKNOWLEDGEMENTS

We thank E. T. Dunham for bringing the Mesquite CAI to our attention and the Center of Meteorite Studies of the Arizona State University for the loan of the NWA 7892 section. This manuscript benefitted from constructive and careful reviews of K. Nagashima and two anonymous reviewers. Editorial handling by Associate Editor Yuri Amelin was greatly appreciated. We are grateful for

[1] Because of the low degrees of freedom (f = 2), the 95% confidence interval around the initial ratio is significantly wider than the 2σ-level uncertainty that is solely based on analytical errors. Assigning uncertainties solely based on analytical errors yields $(^{26}Al/^{27}Al)_0 = (5.4 \pm 0.44) \times 10^{-5}$.

insightful discussions with E. T. Dunham, K. A. McCain, K. D. McKeegan, and H. Tang. Many thanks go to L. Vltava and G. Jarzebinski for keeping the ims-1290 ion probe in top condition and R. Esposito for assistance with EPMA work. This work is supported by the NASA grant 80NSSC18K0602 (to M.-C. Liu). The UCLA ion microprobe facility is partially supported by a grant from the NSF Instrumentation and Facilities program. Noah Bodzin of the UCLA Nanolab facility is thanked for his assistance with FIB operation. We acknowledge the use of facilities within the Eyring Materials Center at Arizona State University supported in part by NNCI-ECCS-1542160.

APPENDIX A. SUPPLEMENTARY MATERIAL

Supplementary data to this article can be found online at https://doi.org/10.1016/j.gca.2020.12.014.

REFERENCES

Amelin Y., Kaltenbach A., Iizuka T., Stirling C. H., Ireland T. R., Petaev M. and Jacobsen S. B. (2010) U–Pb chronology of the Solar System's oldest solids with variable $^{238}U/^{235}U$. *Earth Planet. Sci. Lett.* **300**(3-4), 343–350.

Baertschi P. (1976) Absolute ^{18}O content of standard mean ocean water. *Earth Planet. Sci. Lett.* **31**, 341–344.

Beckett J. R. and Stolper E. (1994) The stability of hibonite, melilite and other aluminous phases in silicate melts: Implications for the origin of hibonite-bearing inclusions from carbonaceous chondrites. *Meteoritics* **29**(1), 41–65.

Boynton W. V. (1989) Cosmochemistry of the rare earth elements: condensation and evaporation processes. *Rev. Mineral. Geochem.* **21**, 1–24.

Brearley A. J. and Jones R. H. (1998) Chondritic Meteorites. *Rev. Mineral. Geochem.* **36**, 3-01–3-398.

Catanzaro E. J., Murphy T. J., Garner E. L. and Shields W. R. (1966) Absolute isotopic abundance ratios and atomic weight of magnesium. *J. Res. Natl. Bur. Stan. Sect. A.* **70A**(6), 453. https://doi.org/10.6028/jres.070A.037.

Clayton R. N., Onuma N., Grossman L. and Mayeda T. K. (1977) Distribution of the pre-Solar component in Allende and other carbonaceous chondrites. *Earth Planet. Sci. Lett.* **34**, 209–224.

Connelly J. N., Bizzarro M., Krot A. N., Nordlund Å., Wielandt D. and Ivanova M. A. (2012) The absolute chronology and thermal processing of solids in the solar protoplanetary disk. *Science* **338**(6107), 651–655. https://doi.org/10.1126/science.1226458.

Connelly J. N., Bollard J. and Bizzarro M. (2017) Pb–Pb chronometry and the early Solar System. *Geochim. Cosmochim. Acta* **201**, 345–363. https://doi.org/10.1016/j.gca.2016.10.044.

Davis A. M., Richter F. M., Mendybaev R. A., Janney P. E., Wadhwa M. and McKeegan K. D. (2015) Isotopic mass fractionation laws for magnesium and their effects on ^{26}Al–^{26}Mg systematics in solar system materials. *Geochim. Cosmochim. Acta* **158**, 245–261. https://doi.org/10.1016/j.gca.2015.01.034.

Defouilloy C., Nakashima D., Joswiak D. J., Brownlee D. E., Tenner T. J. and Kita N. T. (2017) Origin of crystalline silicates from Comet 81P/Wild 2: Combined study on their oxygen isotopes and mineral chemistry. *Earth Planet. Sci. Lett.* **465**, 145–154. https://doi.org/10.1016/j.epsl.2017.02.045.

Doyle P. M., Jogo K., Nagashima K., Krot A. N., Wakita S., Ciesla F. J. and Hutcheon I. D. (2015) Early aqueous activity on the ordinary and carbonaceous chondrite parent bodies recorded by fayalite. *Nat. Commun.* **6**(1). https://doi.org/10.1038/ncomms8444.

El Goresy A., Zinner E., Matsunami S., Palme H., Spettel B., Lin Y. and Nazarov M. (2002) Efremovka 101.1: a CAI with ultrarefractory REE patterns and enormous enrichments of Sc, Zr, and Y in Fassaite and Perovskite. *Geochim. Cosmochim. Acta* **66**(8), 1459–1491.

Farver J. R. (2010) Oxygen and hydrogen diffusion in minerals. *Rev. Mineral. Geochem.* **72**(1), 447–507. https://doi.org/10.2138/rmg.2010.72.10.

Fegley M. B. (1982) Hibonite condensation in the solar nebula. *Lunar Planet. Sci. MCMLXXXI*, 211–212.

Fujiya W., Sugiura N., Sano Y. and Hiyagon H. (2013) Mn–Cr ages of dolomites in CI chondrites and the Tagish Lake ungrouped carbonaceous chondrite. *Earth Planet. Sci. Lett.* **362**, 130–142. https://doi.org/10.1016/j.epsl.2012.11.057.

Fujiya W., Sugiura N., Marrocchi Y., Takahata N., Hoppe P., Shirai K., Sano Y. and Hiyagon H. (2015) Comprehensive study of carbon and oxygen isotopic compositions, trace element abundances, and cathodoluminescence intensities of calcite in the Murchison CM chondrite. *Geochim. Cosmochim. Acta* **161**, 101–117. https://doi.org/10.1016/j.gca.2015.04.010.

Grossman L. (2010) Vapor-condensed phase processes in the early solar system. *Meteorit. Planet. Sci.* **556**, L63. https://doi.org/10.1111/j.1945-5100.2009.01010.x.

Grossman L., Simon S. B., Rai V. K., Thiemens M. H., Hutcheon I. D., Williams R. W., Galy A., Ding T., Fedkin A. V., Clayton R. N. and Mayeda T. K. (2008) Primordial compositions of refractory inclusions. *Geochim. Cosmochim. Acta* **72**(12), 3001–3021. https://doi.org/10.1016/j.gca.2008.04.002.

Grossman L., Ebel D. S., Simon S. B., Davis A. M., Richter F. M. and Parsad N. M. (2000) Major element chemical and isotopic compositions of refractory inclusions in C3 chondrites: the separate roles of condensation and evaporation. *Geochim. Cosmochim. Acta* **64**(16), 2879–2894.

Han J. and Brearley A. J. (2017) Microstructures and formation history of melilite-rich calcium–aluminum-rich inclusions from the ALHA77307 CO3.0 chondrite. *Geochim. Cosmochim. Acta* **201**, 136–154. https://doi.org/10.1016/j.gca.2016.10.014.

Heck P. R., Ushikubo T., Schmitz B., Kita N. T., Spicuzza M. J. and Valley J. W. (2010) A single asteroidal source for extraterrestrial Ordovician chromite grains from Sweden and China: High-precision oxygen three-isotope SIMS analysis. *Geochim. Cosmochim. Acta* **74**(2), 497–509. https://doi.org/10.1016/j.gca.2009.10.027.

Hsu W., Guan Y., Leshin L. A., Ushikubo T. and Wasserburg G. J. (2006) A late episode of irradiation in the early solar system: evidence from extinct ^{36}Cl and ^{26}Al in meteorites. *Astrophys. J.* **640**, 525–529.

Imae N. and Nakamuta Y. (2018) A new mineralogical approach for CO3 chondrite characterization by X-ray diffraction: Identification of primordial phases and thermal history. *Meteorit. Planet. Sci.* **53**, 232–248. https://doi.org/10.1111/maps.12996.

Ireland T. R., Avila J., Greenwood R. C., Hicks L. J. and Bridges J. C. (2020) Oxygen isotopes and sampling of the solar system. *Space Sci. Rev.* **216**(2). https://doi.org/10.1007/s11214-020-0645-3.

Itoh S., Kojima H. and Yurimoto H. (2004) Petrography and oxygen isotopic compositions in refractory inclusions from CO chondrites. *Geochim. Cosmochim. Acta* **68**(1), 183–194. https://doi.org/10.1016/S0016-7037(03)00368-5.

Ito, M., Ganguly, J., 2009. Magnesium diffusion in minerals in CAIs: New experimental data for melilites, implications for the Al-Mg chronometer and thermal history of CAIs. Lunar Planet. Sci. MMIX, abstract #1753.

Ivanova M. A., Krot A. N., Nagashima K. and MacPherson G. J. (2012) Compound ultrarefractory CAI-bearing inclusions from

CV3 carbonaceous chondrites. *Meteorit. Planet. Sci.* **47**, 2107–2127. https://doi.org/10.1111/maps.12031.

Jacobsen B., Yin Q.-Z., Moynier F., Amelin Y., Krot A. N., Nagashima K., Hutcheon I. D. and Palme H. (2008) ^{26}Al–^{26}Mg and ^{207}Pb–^{206}Pb systematics of Allende CAIs: Canonical solar initial ^{26}Al/^{27}Al ratio reinstated. *Earth Planet. Sci. Lett.* **272**(1-2), 353–364. https://doi.org/10.1016/j.epsl.2008.05.003.

Kawasaki N., Itoh S., Sakamoto N. and Yurimoto H. (2017) Chronological study of oxygen isotope composition for the solar protoplanetary disk recorded in a fluffy Type A CAI from Vigarano. *Geochim. Cosmochim. Acta* **201**, 83–102. https://doi.org/10.1016/j.gca.2015.12.031.

Kawasaki N., Wada S., Park C., Sakamoto N. and Yurimoto H. (2020) Variations in initial ^{26}Al/^{27}Al ratios among fine-grained Ca-Al-rich inclusions from reduced CV chondrites. *Geochim. Cosmochim. Acta* **279**, 1–15. https://doi.org/10.1016/j.gca.2020.03.045.

Kita N. T., Huss G. R., Tachibana S., Amelin Y., Nyquist L. E. and Hutcheon I. D. (2005) Constraints on the origin of chondrules and CAIs from short-lived and long-lived radionuclides. In *Chondrites and the Protoplanetary Disk* (eds. A. N. Krot, E. R. D. Scott and B. Reipurth). Astronomical Society of the Pacific, San Francisco, CA, pp. 558–587.

Kita N. T., Nagahara H., Tachibana S., Tomomura S., Spicuzza M. J., Fournelle J. H. and Valley J. W. (2010) High precision SIMS oxygen three isotope study of chondrules in LL3 chondrites: Role of ambient gas during chondrule formation. *Geochim. Cosmochim. Acta* **74**(22), 6610–6635. https://doi.org/10.1016/j.gca.2010.08.011.

Kööp L., Nakashima D., Heck P. R., Kita N. T., Tenner T. J., Krot A. N., Nagashima K., Park C. and Davis A. M. (2016) New constraints on the relationship between ^{26}Al and oxygen, calcium, and titanium isotopic variation in the early Solar System from a multielement isotopic study of spinel-hibonite inclusions. *Geochim. Cosmochim. Acta* **184**, 151–172. https://doi.org/10.1016/j.gca.2016.04.018.

Krot A. N. (2019) Refractory inclusions in carbonaceous chondrites: Records of early solar system processes. *Meteorit. Planet. Sci.* **54**(8), 1647–1691. https://doi.org/10.1111/maps.13350.

Krot A. N. and Nagashima K. (2016) Evidence for oxygen-isotope exchange in chondrules and refractory inclusions during fluid-rock interaction on the CV chondrite parent body. *79th Annual Meeting of the Meteoritical Society Meteorit. Planet. Sci. Suppl.* **51**, abstract #6014.

Krot A. N., Ma C., Nagashima K., Davis A. M., Beckett J. R., Simon S. B., Komatsu M., Fagan T. J., Brenker F., Ivanova M. A. and Bischoff A. (2019a) Mineralogy, petrography, and oxygen isotopic compositions of ultrarefractory inclusions from carbonaceous chondrites. *Geochemistry* **79**(4), 125519. https://doi.org/10.1016/j.chemer.2019.07.001.

Krot A. N., Nagashima K., Simon S. B., Ma C., Connolly, Jr., H. C., Huss G. R., Davis A. M. and Bizzarro M. (2019b) Mineralogy, petrography, and oxygen and aluminum-magnesium isotope systematics of grossite-bearing refractory inclusions. *Geochemistry* **79**(4), 125529. https://doi.org/10.1016/j.chemer.2019.08.001.

Krot A. N., Nagashima K., Fintor K. and Pál-Molnár E. (2019c) Evidence for oxygen-isotope exchange in refractory inclusions from Kaba (CV3.1) carbonaceous chondrite during fluid-rock interaction on the CV parent asteroid. *Geochim. Cosmochim. Acta* **246**, 419–435. https://doi.org/10.1016/j.gca.2018.11.002.

Larsen K. K., Trinquier A., Paton C., Schiller M., Wielandt D., Ivanova M. A., Connelly J. N., Nordlund Å., Krot A. N. and Bizzarro M. (2011) Evidence for magnesium isotope heterogeneity in the solar protoplanetary disk. *Astrophys. J.* **735**, L37. https://doi.org/10.1088/2041-8205/735/2/L37.

Larsen K. K., Wielandt D., Schiller M., Krot A. N. and Bizzarro M. (2020) Episodic formation of refractory inclusions in the Solar System and their presolar heritage. *Earth Planet. Sci. Lett.* **535**, 116088. https://doi.org/10.1016/j.epsl.2020.116088.

Lagerlof K. P. D., Mitchell T. E. and Heuer A. H. (1989) Lattice diffusion kinetics in undoped and impurity-doped sapphire (α-Al_2O_3): A dislocation loop annealing study. *J. Am. Ceram. Soc.* **72**, 2159–2171.

Lin Y., Guan Y., Leshin L. A., Ouyang Z. and Wang D. (2005) Short-lived chlorine-36 in a Ca- and Al-rich inclusion from the Ningqiang carbonaceous chondrite. *Proc. Natl. Acad. Sci.* **102**(5), 1306–1311.

Liu M.-C., McKeegan K. D., Goswami J. N., Marhas K. K., Sahijpal S., Ireland T. R. and Davis A. M. (2009) Isotopic records in CM hibonites: Implications for timescales of mixing of isotope reservoirs in the solar nebula. *Geochim. Cosmochim. Acta* **73**(17), 5051–5079. https://doi.org/10.1016/j.gca.2009.02.039.

Liu M.-C., McKeegan K. D., Harrison T. M., Jarzebinski G. and Vltava L. (2018) The Hyperion-II radio-frequency oxygen ion source on the UCLA ims1290 ion microprobe: Beam characterization and applications in geochemistry and cosmochemistry. *Int. J. Mass Spectrom.* **424**, 1–9. https://doi.org/10.1016/j.ijms.2017.11.007.

Liu M.-C., Han J., Brearley A. J. and Hertwig A. T. (2019) Aluminum-26 chronology of dust coagulation and early solar system evolution. *Sci. Adv.* **5**, 1–8.

Lodders K. (2003) Solar system abundances and condensation temperatures of the elements. *Astrophys. J.* **591**, S. 1220–1247.

Ma C., Kampf A. R., Connolly H. C., Beckett J. R., Rossman G. R., Smith S. A. S. and Schrader D. L. (2011) Krotite, $CaAl_2O_4$, a new refractory mineral from the NWA 1934 meteorite. *Am. Mineral.* **96**(5-6), 709–715. https://doi.org/10.2138/am.2011.3693.

Ma C., Tschauner O., Beckett J. R., Rossman G. R. and Liu W. (2012) Panguite, $(Ti^{4+},Sc,Al,Mg,Zr,Ca)_{1.8}O_3$, a new ultrarefractory titania mineral from the Allende meteorite: Synchrotron micro-diffraction and EBSD. *Am. Mineral.* **97**(7), 1219–1225. https://doi.org/10.2138/am.2012.4027.

Ma C., Tschauner O., Beckett J. R., Rossman G. R. and Liu W. (2013) Kangite, $(Sc, Ti, Al, Zr, Mg, Ca)_2O_3$, a new ultrarefractory scandia mineral from the Allende meteorite: Synchrotron micro-Laue diffraction and electron backscatter diffraction. *Am. Mineral.* **98**(5–6), 870–878. https://doi.org/10.2138/am.2013.4290.

Ma C., Krot A. N., Beckett J. R., Nagashima K. and Tschauner O. (2015) Discovery of warkite, $Ca_2Sc_6Al_6O_{20}$, a new Sc-rich ultrarefractory mineral in Murchison and Vigarano. *Lunar Planet. Sci. MMXV*, abstract #5025.

Ma C., Krot A. N., Beckett J. R., Nagashima K., Tschauner O., Rossman G. R., Simon S. B. and Bischoff A. (2020) Warkite, $Ca_2Sc_6Al_6O_{20}$, a new mineral in carbonaceous chondrites and a key-stone phase in ultrarefractory inclusions from the solar nebula. *Geochim. Cosmochim. Acta* **277**, 52–86. https://doi.org/10.1016/j.gca.2020.03.002.

MacPherson G. J. (2014) Calcium–aluminum-rich inclusions in chondritic meteorites. In *Treatise on Geochemistry* (eds. H. D. Holland and K. K. Turekian). Elsevier, Amsterdam, pp. 139–179.

Macpherson G. J. and Grossman L. (1984) "Fluffy" Type A Ca-, Al-rich inclusions in the Allende meteorite. *Geochim. Cosmochim. Acta* **48**(1), 29–46. https://doi.org/10.1016/0016-7037(84)90347-8.

MacPherson G. J., Davis A. M. and Zinner E. K. (1995) The distribution of aluminum-26 in the early Solar System-A reappraisal. *Meteoritics* **30**(4), 365–386.

MacPherson G. J., Kita N. T., Ushikubo T., Bullock E. S. and Davis A. M. (2012) Well-resolved variations in the formation ages for Ca–Al-rich inclusions in the early Solar System. *Earth Planet. Sci. Lett.* **331-332**, 43–54. https://doi.org/10.1016/j.epsl.2012.03.010.

MacPherson G. J., Bullock E. S., Tenner T. J., Nakashima D., Kita N. T., Ivanova M. A., Krot A. N., Petaev M. I. and Jacobsen S. B. (2017) High precision Al–Mg systematics of forsterite-bearing Type B CAIs from CV3 chondrites. *Geochim. Cosmochim. Acta* **201**, 65–82. https://doi.org/10.1016/j.gca.2016.12.006.

Mahon K. I. (1996) The New "York" regression: Application of an improved statistical method to geochemistry. *Int. Geol. Rev.* **38** (4), 293–303.

Makide K., Nagashima K., Krot A. N., Huss G. R., Hutcheon I. D. and Bischoff A. (2009) Oxygen- and magnesium-isotope compositions of calcium–aluminum-rich inclusions from CR2 carbonaceous chondrites. *Geochim. Cosmochim. Acta* **73**(17), 5018–5050. https://doi.org/10.1016/j.gca.2009.01.042.

Makide K., Nagashima K., Krot A. N., Huss G. R., Ciesla F. J., Hellebrand E., Gaidos E. and Yang L. (2011) Heterogeneous distribution of 26-Al at the birth of the solar system. *Astrophys. J.* **733**, L31.

McCain K. A., McKeegan K. D., Young E. D., Brearley A. J. and Alexander C. M. O'D. (2018) Fluid evolution on carbonaceous asteroids: Interrogating the carbonate record. In *81st Annual Meteoritical Society Meeting Meteorit. Planet. Sci. Suppl.*, p. 6172.

Mendybaev R. A., Richter F. M. and Davis A. M. (2006) Crystallization of melilite from CMAS-liquids and the formation of the melilite mantle of Type B1 CAIs: Experimental simulations. *Geochim. Cosmochim. Acta* **70**, 2622–2642. https://doi.org/10.1016/j.gca.2006.02.018.

Mishra R. K. (2018) Petrography and mineralogy of calcium-, aluminum-rich inclusions in an unequilibrated carbonaceous chondrite Y 81020 (CO3.05). *Curr. Sci.* **114**, 1510–1519.

Nakashima D., Ushikubo T., Joswiak D. J., Brownlee D. E., Matrajt G., Weisberg M. K., Zolensky M. E. and Kita N. T. (2012) Oxygen isotopes in crystalline silicates of comet Wild 2: A comparison of oxygen isotope systematics between Wild 2 particles and chondritic materials. *Earth Planet. Sci. Lett.* **357–358**, 355–365. https://doi.org/10.1016/j.epsl.2012.09.041.

Norris T. L., Gancarz A. J., Rokop D. J. and Thomas K. W. (1983) Half-Life of ^{26}Al. *J. Geophys. Res.* **88**, B331–B333.

Park C., Wakaki S. and Yurimoto H. (2012) Oxygen isotopic variations in a type A Ca-Al-rich inclusion revealed by high-precision secondary ion mass spectrometry analysis with micrometer resolution. *Surf. Interface Anal.* **44**, 678–681. https://doi.org/10.1002/sia.3871.

Park C., Ivanova M. A., Nagashima K., Krot A. N. and MacPherson G. J. (2014) Al-Mg systematics of ultrarefractory CAIs from CV3 chondrites. *77th Annual Meteoritical Society Meeting Meteorit. Planet. Sci. Suppl.* **49**, abstract #5098.

Richter F. M., Davis A. M., Ebel D. S. and Hashimoto A. (2002) Elemental and isotopic fractionation of Type B calcium-, aluminum-rich inclusions: Experiments, theoretical considerations, and constraints on their thermal evolution. *Geochim. Cosmochim. Acta* **66**, 521–540.

Richter F. M., Janney P. E., Mendybaev R. A., Davis A. M. and Wadhwa M. (2007) Elemental and isotopic fractionation of Type B CAI-like liquids by evaporation. *Geochim. Cosmochim. Acta* **71**, 5544–5564. https://doi.org/10.1016/j.gca.2007.09.005.

Russell S. S., Huss G. R., Fahey A. J., Greenwood R. C., Hutchison R. and Wasserburg G. J. (1998) An isotopic and petrologic study of calcium-aluminum-rich inclusions from CO3 meteorites. *Geochim. Cosmochim. Acta* **62**(4), 689–714. https://doi.org/10.1016/S0016-7037(97)00374-8.

Ryerson F. J. and McKeegan K. D. (1994) Determination of oxygen self-diffusion in ikermanite, anorthite, diopside, and spinel: Implications for oxygen isotopic anomalies and the thermal histories of Ca-Al-rich inclusions. *Geochim. Cosmochim. Acta* **58**, 3713–3734.

Schwinger S., Dohmen R. and Schertl H.-P. (2016) A combined diffusion and thermal modeling approach to determine peak temperatures of thermal metamorphism experienced by meteorites. *Geochim. Cosmochim. Acta* **191**, 255–276. https://doi.org/10.1016/j.gca.2016.06.015.

Scott E. R. D. and Krot A. N. (2014) Chondrites and their components. In *Treatise on Geochemistry* (eds. H. D. Holland and K. K. Turekian). Elsevier, Amsterdam, pp. 65–137.

Simon S. B., Davis A. M. and Grossman L. (1999) Origin of compact type A refractory inclusions from CV3 carbonaceous chondrites. *Geochim. Cosmochim. Acta* **63**, 1233–1248.

Simon S. B., Krot A. N., Nagashima K., Kööp L. and Davis A. M. (2019a) Condensate refractory inclusions from the CO3.00 chondrite Dominion Range 08006: Petrography, mineral chemistry, and isotopic compositions. *Geochim. Cosmochim. Acta* **246**, 109–122. https://doi.org/10.1016/j.gca.2018.11.029.

Simon S. B., Krot A. N. and Nagashima K. (2019b) Oxygen and Al-Mg isotopic compositions of grossite-bearing refractory inclusions from CO3 chondrites. *Meteorit. Planet. Sci.* **54**, 1362–1378. https://doi.org/10.1111/maps.13282.

Stolper E. (1982) Crystallization sequences of Ca-Al-rich inclusions from Allende: An experimental study. *Geochim. Cosmochim. Acta* **46**, 2159–2180.

Stolper E. and Paque J. M. (1986) Crystallization sequences of Ca-Al-rich inclusions from Allende: The effects of cooling rate and maximum temperature. *Geochim. Cosmochim. Acta* **50**, 1785–1806.

Tang H., Liu M.-C., McKeegan K. D., Tissot F. L. H. and Dauphas N. (2017) In situ isotopic studies of the U-depleted Allende CAI Curious Marie: Pre-accretionary alteration and the co-existence of ^{26}Al and ^{36}Cl in the early solar nebula. *Geochim. Cosmochim. Acta* **207**, 1–18. https://doi.org/10.1016/j.gca.2017.03.001.

Trappitsch R., Boehnke P., Stephan T., Telus M., Savina M. R., Pardo O., Davis A. M., Dauphas N., Pellin M. J. and Huss G. R. (2018) New constraints on the abundance of 60Fe in the early solar system. *Astrophys. J.* **857**, L15. https://doi.org/10.3847/2041-8213/aabba9.

Ushikubo T., Kimura M., Kita N. T. and Valley J. W. (2012) Primordial oxygen isotope reservoirs of the solar nebula recorded in chondrules in Acfer 094 carbonaceous chondrite. *Geochim. Cosmochim. Acta* **90**, 242–264. https://doi.org/10.1016/j.gca.2012.05.010.

Ushikubo T., Tenner T. J., Hiyagon H. and Kita N. T. (2017) A long duration of the ^{16}O-rich reservoir in the solar nebula, as recorded in fine-grained refractory inclusions from the least metamorphosed carbonaceous chondrites. *Geochim. Cosmochim. Acta* **201**, 103–122. https://doi.org/10.1016/j.gca.2016.08.032.

Wasserburg G. J., Wimpenny J. and Yin Q.-Z. (2012) Mg isotopic heterogeneity, Al-Mg isochrons, and canonical 26Al/27Al in the early solar system. *Meteorit. Planet. Sci.* **47**, 1980–1997. https://doi.org/10.1111/maps.12014.

Wasson J. T., Yurimoto H. and Russel S. S. (2001) ^{16}O-rich melilite in CO3.0 chondrites: Possible formation of common, ^{16}O-poor melilite by aqueous alteration. *Geochim. Cosmochim. Acta* **65**, 4539–4549.

Young E. D. and Galy A. (2004) The isotope geochemistry and cosmochemistry of magnesium. *Rev. Mineral. Geochem.* **55**(1), 197–230. https://doi.org/10.2138/gsrmg.55.1.197.

Yurimoto H., Morioka M. and Nagasawa H. (1989) Diffusion in single crystals of melilite: I. Oxygen. *Geochim. Cosmochim. Acta* **53**, 2387–2394. https://doi.org/10.1016/0016-7037(89)90360-8.

Yurimoto H., Krot A. N., Choi B.-G., Aleon J., Kunihiro T. and Brearley A. J. (2008) Oxygen isotopes of chondritic components. *Rev. Mineral. Geochem.* **68**(1), 141–186. https://doi.org/10.2138/rmg.2008.68.8.

Zhang A.-C., Ma C., Sakamoto N., Wang R.-C., Hsu W.-B. and Yurimoto H. (2015) Mineralogical anatomy and implications of a Ti–Sc-rich ultrarefractory inclusion from Sayh al Uhaymir 290 CH3 chondrite. *Geochim. Cosmochim. Acta* **163**, 27–39. https://doi.org/10.1016/j.gca.2015.04.052.

Zhang M., Bonato E., King A. J., Russell S. S., Tang G. and Lin Y. (2020) Petrology and oxygen isotopic compositions of calcium-aluminum-rich inclusions in primitive CO3.0-3.1 chondrites. *Meteorit. Planet. Sci.* **55**, 911–935. https://doi.org/10.1111/maps.13473.

Zhi W., Wang F., Yang B., Qu T., Deng Y., Tian Y. and Zhao J. (2019) Phase relations of CaO-Al_2O_3-Sc_2O_3 ternary system. *J. Am. Ceram. Soc.* **102**, 2863–2870. https://doi.org/10.1111/jace.16104.

Associate editor: Yuri Amelin